Off-Equatorial Deep-Cycle Turbulence Forced by Tropical Instability Waves in the Equatorial Pacific

D. A. CHERIAN,[a] D. B. WHITT,[a,b] R. M. HOLMES,[c,d,e] R.-C. LIEN,[f,g] S. D. BACHMAN,[a] AND W. G. LARGE[a]

[a] *National Center for Atmospheric Research, Boulder, Colorado*
[b] *Earth Sciences Division, NASA Ames Research Center, Moffett Field, California*
[c] *Climate Change Research Centre, University of New South Wales, Sydney, New South Wales, Australia*
[d] *School of Mathematics and Statistics, University of New South Wales, Sydney, New South Wales, Australia*
[e] *ARC Centre of Excellence for Climate Extremes, University of New South Wales, Sydney, New South Wales, Australia*
[f] *Applied Physics Laboratory, University of Washington, Seattle, Washington*
[g] *School of Oceanography, University of Washington, Seattle, Washington*

(Manuscript received 21 September 2020, in final form 16 February 2021)

ABSTRACT: The equatorial Pacific cold tongue is a site of large heat absorption by the ocean. This heat uptake is enhanced by a daily cycle of shear turbulence beneath the mixed layer—''deep-cycle turbulence''—that removes heat from the sea surface and deposits it in the upper flank of the Equatorial Undercurrent. Deep-cycle turbulence results when turbulence is triggered daily in sheared and stratified flow that is marginally stable (gradient Richardson number Ri ≈ 0.25). Deep-cycle turbulence has been observed on numerous occasions in the cold tongue at 0°, 140°W, and may be modulated by tropical instability waves (TIWs). Here we use a primitive equation regional simulation of the cold tongue to show that deep-cycle turbulence may also occur off the equator within TIW cold cusps where the flow is marginally stable. In the cold cusp, preexisting equatorial zonal shear u_z is enhanced by horizontal vortex stretching near the equator, and subsequently modified by horizontal vortex tilting terms to generate meridional shear v_z off of the equator. Parameterized turbulence in the sheared flow of the cold cusp is triggered daily by the descent of the surface mixing layer associated with the weakening of the stabilizing surface buoyancy flux in the afternoon. Observational evidence for off-equatorial deep-cycle turbulence is restricted to a few CTD casts, which, when combined with shear from shipboard ADCP data, suggest the presence of marginally stable flow in TIW cold cusps. This study motivates further observational campaigns to characterize the modulation of deep-cycle turbulence by TIWs both on and off the equator.

KEYWORDS: Pacific Ocean; Tropics; Mixing; Turbulence

1. Introduction

The equatorial Pacific cold tongue is a zonal band of cold upper-ocean water in the eastern equatorial Pacific extending between the Pacific's eastern margin and approximately 155°W. Being cold water in a region of large solar insolation, the cold tongue is a region of large heat absorption by the ocean between approximately 3°S and 3°N (e.g., Large and Yeager 2009; Holmes et al. 2019). Absorbing such a large amount of heat while maintaining cold sea surface temperatures (SSTs) is only possible if the heat taken in by the ocean is quickly transported away from the equatorial sea surface. Mixed layer heat budgets for the eastern Pacific constructed using equatorial mooring observations show that the downward transport of heat by microscale turbulence is essential to keeping the sea surface cool (Moum et al. 2013; Wang and McPhaden 1999, 2000; Warner and Moum 2019; Ray et al. 2018). The annual cycle of turbulence is strong enough that there is only a single peak in the annual cycle of equatorial sea surface temperature (SST) despite a double peak in solar insolation as the sun ''crosses'' the equator twice through the year (Moum et al. 2013). On longer time scales, the rate of change of SST during ENSO phase transitions approximately agrees with both amplitude and phase of turbulence heat flux divergence across the mixed layer (Warner and Moum 2019). Equatorial mixing might be critical to one of Earth's most consequential climate phenomena. Yet little is known about its spatial structure with current observations restricted to a few sites along the equator.

The microstructure observations that do exist have illustrated the complex nature of equatorial turbulence. At the equator, winds maintain a strong zonal mean flow with intense vertical shear between the eastward flowing Equatorial Undercurrent (EUC) at depth and the westward flowing near-surface South Equatorial Current (SEC). Observations at 0°, 140°W repeatedly show the existence of diurnally modulated shear-driven turbulence beneath the base of the mixed layer in the high shear zone above the core of the EUC—''deep-cycle turbulence'' (Gregg et al. 1985; Moum and Caldwell 1985; Lien et al. 1995; Moum et al. 2009). In this deep-cycle layer the flow's gradient Richardson number,

$$\mathrm{Ri} = b_z/(u_z^2 + v_z^2), \tag{1}$$

(where $b = -g\rho/\rho_0$ is buoyancy, u and v are the horizontal components of velocity, and subscripts indicate differentiation), remains near its critical value of 0.25 throughout the year. That is, this layer is marginally stable to shear instability (Thorpe and Liu 2009; Smyth and Moum 2013; Pham et al. 2017; Smyth et al. 2019).

Corresponding author: Deepak A. Cherian, deepak@cherian.net

DOI: 10.1175/JPO-D-20-0229.1

A daily cycle of turbulence requires a diurnal trigger in the marginally stable layer. At least two hypotheses have been proposed for this diurnal trigger. A number of authors (e.g., Wijesekera and Dillon 1991; Peters et al. 1994) propose that downward-propagating internal waves, excited at the base of the mixed layer during nighttime convection, break in the marginally stable layer and trigger turbulence. However, the 1D model solutions of Schudlich and Price (1992) suggested that the diurnal trigger is the descent of the daytime shear layer formed by the trapping of momentum in a near-surface stratified layer. Their model result supported observations reported in Smyth and Moum (2013).

As the near-surface stratification built up by solar radiation during the day decreases in the afternoon the warm-layer jet goes unstable, triggering turbulence at the base of the mixed layer in large-eddy simulations (Pham et al. 2017). This turbulence transports momentum downward, locally increasing shear in the marginally stable layer, reducing Ri and triggering further shear instability. As this process continues, the envelope of actively turbulent fluid propagates downward and is visible as a downward descent of a local maximum in vertical shear (Smyth et al. 2013). Turbulence persists during the next morning at depths up to 80–100 m at 0°, 140°W despite the cessation of near-surface convection; and increases Ri back to its marginally stable value of approximately 0.25 at which point turbulence decays. Smyth et al. (2019) argue that turbulent diffusion tends to reduce buoyancy and velocity gradients, b_z and u_z, at roughly similar rates so $\mathrm{Ri} = b_z/u_z^2$ must increase. In this way flow in the deep-cycle layer is restored to a state of marginal stability ($\mathrm{Ri} \approx 0.25$). Near-surface turbulence is then triggered in the late afternoon and the cycle repeats. Large-eddy simulations initialized with mean fields representative of each of the four seasons show that deep-cycle turbulence exists throughout the year, though the depth to which it penetrates varies with the seasonal shoaling and deepening of the EUC (Pham et al. 2017). Mooring observations in the Atlantic Ocean (Wenegrat and McPhaden 2015), ship-based microstructure measurements in the Indian Ocean (Pujiana et al. 2018), and a global primitive equation simulation using a k–ε turbulence closure model (Pei et al. 2020) suggest that deep-cycle turbulence may also exist in the equatorial Atlantic and Indian Oceans. These studies have all focused on deep-cycle turbulence right at the equator.

The equatorial Pacific is also the site of energetic mesoscale variability in the form of tropical instability waves (TIWs). TIWs are formed through barotropic and baroclinic instability of the equatorial current system, and manifest as a series of westward traveling cold cusps and warm troughs. TIWs have zonal wavelengths of 1000–2000 km, periods of 15–40 days, and propagate westward with a phase speed of approximately $0.5\ \mathrm{m\,s^{-1}}$ (Philander 1976; Legeckis 1977; Qiao and Weisberg 1995; Chelton et al. 2000; Lyman et al. 2005; Holmes and Thomas 2016). The cold cusps of TIWs exhibit vigorous circulation features with sharp fronts and convergence zones that influence biological activity (Yoder et al. 1994; Strutton et al. 2001; Warner et al. 2018).

TIWs may modulate cold tongue turbulence. Lien et al. (2008) reported intense mixing at the base of the mixed layer recorded by a Lagrangian float that meandered through two TIWs between 2°S and 1°N in 2005 with a peak heat flux estimate of $1000\ \mathrm{W\,m^{-2}}$. During the EQUIX experiment at 0°, 140°W in 2008, a La Niña year, turbulent heat fluxes at the equator reached $400\ \mathrm{W\,m^{-2}}$ when averaged over 2 weeks (Moum et al. 2009) in the presence of TIWs, compared to the approximately $50\ \mathrm{W\,m^{-2}}$ measured previously (Lien et al. 1995). The base of the marginally stable layer appears to shallow by a factor of 2 to 50 m during the warm phase of the TIW as compared to that during the cold phase (Moum et al. 2009; Inoue et al. 2012, 2019). Recent work with TAO observations indicates that a subsurface mode of TIWs (Liu et al. 2019) as well as equatorial inertial gravity waves at periods between 3 and 25 days (Liu et al. 2020) may strongly influence the vertical structure of shear and thereby diapycnal mixing at the equator, consistent with (Moum et al. 2009; Inoue et al. 2019). Note that microstructure profiler observations have not yet captured one entire TIW period. These observations are consistent with modeling studies that show enhanced turbulence both at the equator during particular TIW phases (Menkes et al. 2006; Holmes and Thomas 2015). Holmes and Thomas (2015) proposed a dynamical explanation for the enhancement of equatorial turbulence by TIWs: meridional diffluence (positive v_y) of TIW flow at the equator during the cold phase stretches the southward-oriented meridional component of horizontal vorticity ($\omega^y = w_x - u_z$). The stretching increases $|\omega^y|$, intensifies the preexisting EUC shear u_z at the equator, and forces intense turbulence. During the warm phase, the reverse happens: vortex tubes are squashed and u_z weakens with a corresponding weakening of turbulence. Observational evidence for this mechanism is inconclusive, due in part to the difficulty in obtaining an observational estimate of v_y (Inoue et al. 2019). TIWs also change the latitudinal scale of equatorial mixing: the simulations of both Menkes et al. (2006) and Holmes and Thomas (2015) show the presence of intense mixing in TIW cold cusps off the equator. But, most equatorial microstructure measurements have been made right at the equator, primarily at 0°, 140°W in the Pacific. This sampling bias means that large unknowns remain in our knowledge of the spatial distribution of equatorial upper-ocean mixing.

Here we use a 1/20° regional model of the cold tongue to study how TIWs modulate turbulence off the equator. The simulated TIWs force off-equatorial marginally stable flow and deep-cycle turbulence by generating intense meridional shear (v_z) in the eastward extension of a TIW's cold cusp (sections 3 and 4). This shear results from the rotation or tilting of horizontal vorticity generated by horizontal vortex stretching at the equator (section 4b). Indirect observational evidence for this TIW-forced off-equatorial deep-cycle turbulence is presented through Ri profiles from three cruise sections through TIWs at 110°W (section 5). Our results emphasize the need to observe turbulence variability off the equator; to validate the results presented here, to assess the accuracy of turbulence parameterization schemes in simulating TIW modulated deep-cycle turbulence, and to fully characterize the role of deep-cycle turbulence in the heat budget of the cold tongue.

2. Methods

a. Model configuration

We use a regional configuration of the MITgcm (Marshall et al. 1997; Adcroft et al. 2004) to model the equatorial Pacific cold tongue using NCAR's Cheyenne cluster (Computational And Information Systems Laboratory 2019). The domain extends from 170° to 95°W, 12°S to 12°N with a horizontal grid spacing of 1/20°. There are 345 vertical levels with a spacing of 1 m in the top 250 m that increases to a maximum of 250 m. The model is forced at the surface with fields from the JRA-55do reanalysis (Tsujino et al. 2018) and lateral boundary conditions are specified using daily averaged fields from the Mercator GLORYS12V1 1/12° ocean reanalysis product (Copernicus identifier GLOBAL_REANALYSIS_PHY_001_030). The simulated time period is from 1 September 1995 to 28 February 1997. There is no tidal forcing. The time axis, when presented in figures, is local time at 110°W, chosen to be UTC − 7.

Subgrid-scale vertical mixing is parameterized using the K-profile parameterization (KPP) scheme of Large et al. (1994) with standard parameter values (Large and Gent 1999). The KPP turbulence scheme divides the water column into three parts: an interior region, a boundary layer, and a surface layer (defined to be the top 10% of the boundary layer near the surface). The KPP boundary layer depth H_{KPP} is usually chosen as the depth at which the *bulk* Richardson number

$$\mathrm{Ri}_b = \frac{bH_{0.3}}{|V|^2 + V_t^2(H_{0.3})} \tag{2}$$

exceeds a critical value chosen to be 0.3 ($H_{0.3}$). Here b and V are the differences between values of resolved buoyancy b and resolved velocity V at the surface and at the base of the boundary layer $z = H_{0.3}$. V_t represents a parameterized velocity due to unresolved turbulent eddies. In addition, H_{KPP} is restricted to be less that the Monin–Obukhov length scale

$$L_{\mathrm{MO}} = \frac{-u_*^3}{\kappa B_0}, \tag{3}$$

so that

$$H_{\mathrm{KPP}} = \min[L_{\mathrm{MO}}, H_{0.3}]. \tag{4}$$

Here $u_* = \sqrt{\tau/\rho_0}$ is the friction velocity where τ is the wind stress, B_0 is the surface buoyancy flux, and $\kappa = 0.4$ is the von Kármán constant. Below H_{KPP}, diffusion due to shear instabilities is parameterized using a diffusivity that is a smooth function of gradient Richardson number Ri. This function is nonzero for Ri < 0.7 (Large et al. 1994, their Fig. 3). The shear mixing scheme's parameters were specifically tuned to reproduce the onset of nighttime convection relative to LES (Large and Gent 1999).

b. Model validation

The model simulates the equatorial Pacific reasonably well (Fig. 1). The model fields are compared with the Johnson et al. (2002) climatology and an annual mean climatology constructed using TAO mooring observations in the 1990–2000 decade at 110°W. At the equator, the EUC maximum is approximately 15–20 m deeper than the TAO data and the Johnson et al. (2002) climatology (Fig. 1b), though the depth-integrated zonal velocity in the top 250 m is comparable to that from the Johnson climatology (Fig. 1c). There is a subsurface warm bias relative to both observational datasets (Figs. 1a,e). This subsurface warm bias extends from about 6°S and 6° N, where the top 75 m are slightly less stratified in temperature than observed.

c. Diagnostics

All derivatives in presented terms are estimated using centered differences. Ri is masked out when $N^2 < 10^{-6}\,\mathrm{s}^{-2}$ or $S^2 < 10^{-6}\,\mathrm{s}^{-2}$. The mixed layer depth z_{MLD} is computed as the shallowest depth at which the density exceeds the surface density by 0.015 kg m^{-3}. The base of the deep-cycle layer z_{Ri} is computed as the shallowest depth below the mixed layer base when Ri exceeds 0.5. Our choice of 0.5 instead of 0.25 is discussed in section 3. The thickness of the low Richardson number layer or ''low Ri layer'' is defined as $H = z_{\mathrm{MLD}} - z_{\mathrm{Ri}}$. The parameterized turbulent heat flux $J_q^t = -\rho_0 c_p K_T(T_z - \gamma_T)$, where c_p is the specific heat capacity of water, and γ_T is a nonlocal transport that is nonzero only during convective forcing conditions [Large et al. 1994, their Eqs. (19), (20)]. Negative values of J_q^t indicate heat moving downward.

3. TIW modulated turbulence in the cold tongue

TIW variability imprints itself strongly on SST, surface heat fluxes, and subsurface turbulent mixing both on and off the equator (Fig. 2). The cold tongue, structured by TIW cold cusps, is characterized by strong heat absorption at the surface (positive Q_{net} in Fig. 2a) and intense downward turbulent heat fluxes in the thermocline (Fig. 2d). The low Ri layer also coincides with the cold tongue suggesting both TIW influence and the existence of intense vertical mixing (Fig. 2e). In contrast, the EUC does not coincide with the cold tongue; it is concentrated in an approximately 1° wide latitudinal band around the equator, particularly to the east of 125°W (Fig. 2c). The off-equatorial low Ri flow (Fig. 2e) and associated turbulent heat fluxes (Fig. 2d) cannot be directly associated with shear in the EUC.

Though this manuscript subsequently focuses on one particular TIW to elucidate the processes driving the turbulent heat fluxes below the cold tongue, the correlation between low Ri flow off the equator and cold SSTs associated with TIWs is visible throughout the simulation at 110°, 125°, 140°, and 155°W (Fig. 3). Low Ri values are more common north of the equator than south of the equator, and the latitudinal extent of low Ri flow widens toward the west. These patterns match those of SST and are seen outside the latitudinal extent of the EUC (black lines in Fig. 3). Later during the season (January–March) TIW amplitudes weaken, and clear cusps are not visible in SST. Even then low Ri values are still visible off the equator where relatively cold SSTs are present (e.g., at 110°W in March; Figs. 3a,b) These patterns are qualitatively similar to those in Figs. 2d and 2e. The rest of this manuscript focuses on one representative TIW highlighted by the black box in Fig. 2d.

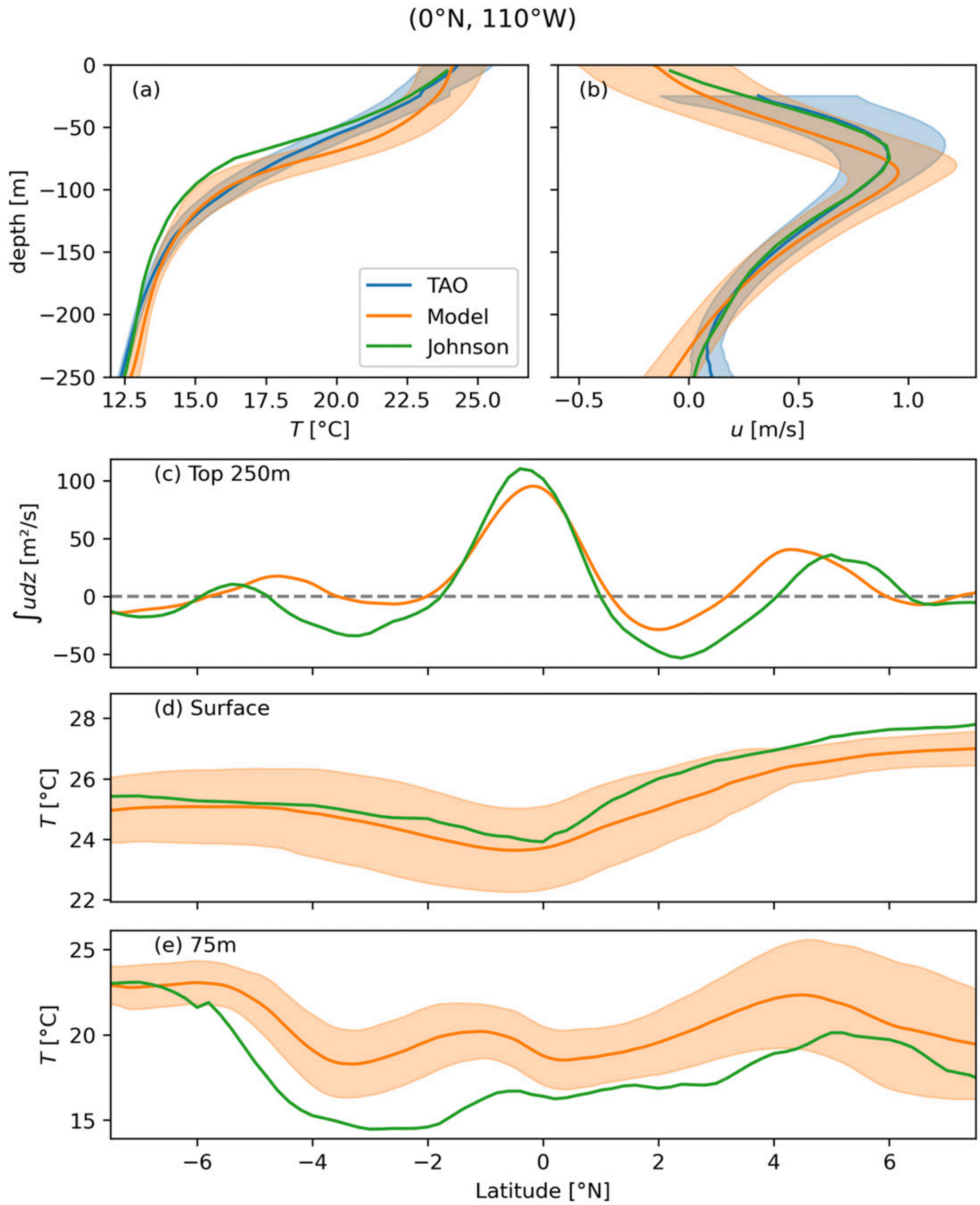

FIG. 1. Comparisons between modeled and observed zonal velocity and temperature at 110°W. (a),(b) Annual mean fields (solid line) and standard deviation of daily means over a year (shaded) for three datasets: the model during 1996 (orange), a climatological annual cycle constructed from the TAO dataset between 1990 and 2000 (blue), and the Johnson et al. (2002) climatology (green, no standard deviation available). (c) Vertically integrated zonal velocity in the top 250 m from the model and the Johnson dataset. Meridional section of temperature at (d) the surface and (e) 75 m.

The vertical structure of mixing associated with this particular TIW at 110°W (black box in Fig. 2d) shows a deep cycle of mixing both on and off the equator at 3.5°N (Figs. 4c,e). At both latitudes, there is a daily cycle in the parameterized turbulent heat flux beneath the mixed layer base (z_{MLD}; orange line in Figs. 2c and 2e) and above the base of the low Ri layer (z_{Ri}; black line in Figs. 2c and 2e). At the equator, z_{Ri} shallows during the TIW warm phase as observed and described by Inoue et al. (2012, 2019) and Moum et al. (2009). At 3.5°N, deep-cycle turbulence starts when the cold cusp reaches that latitude (around 26 November), and persist over the approximately 2-week time period during which the TIW cold cusp reaches this latitude. There is almost no turbulence beneath the mixed layer prior to the arrival of the cold cusp and after its

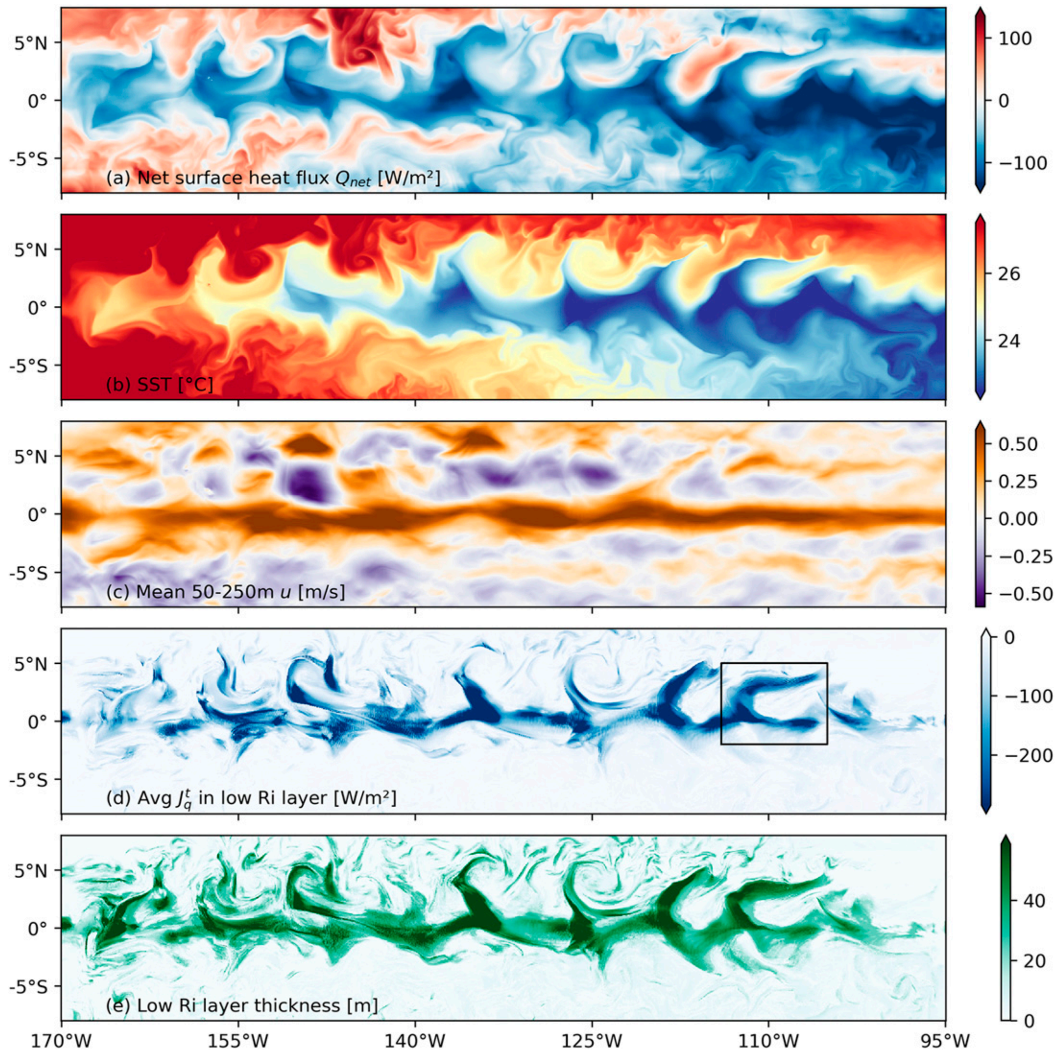

FIG. 2. Daily averaged fields for 5 Dec 1995. (a) Net surface heat flux Q_{net} (negative means heat enters the ocean). (b) SST. (c) Mean zonal velocity between 50 and 250 m. (d) Integrated turbulent heat flux in the low Ri layer ($z_{\mathrm{Ri}} \leq Z < z_{\mathrm{MLD}}$) normalized by a depth of 50 m. (e) Thickness of the low Ri layer ($z_{\mathrm{MLD}} - z_{\mathrm{Ri}}$). The black rectangle in (d) marks the TIW that is studied in detail later in this paper (e.g., Fig. 4).

departure. Daily cycles are also visible in Ri, S^2, N^2 at 3.5°N beneath the mixed layer base for the time period when deep-cycle turbulence is active (Fig. 5). Such daily cycles in shear, stratification and Ri are qualitatively similar to observations and LES at 0°, 140°W (Moum et al. 2009; Pham et al. 2017).

A robust feature of observed deep-cycle layers at the equator is a median Ri of 0.25 (Smyth and Moum 2013; Pham et al. 2017). In the *simulated* deep-cycle layer both on and off the equator, Ri is indeed low, similar to observations, but the median value is higher at about 0.4, a notable bias (Figs. 4d,f), suggesting that the KPP mixing scheme is too diffusive. This may be partly responsible for the subsurface warm bias in Fig. 1e. The critical Ri bias may partly arise because KPP's shear mixing scheme parameterizes diffusivity K_T as a smooth function of Ri that is nonzero for Ri < 0.7 (Large et al. 1994). This function lacks a rapid transition in diffusivity as Ri reduces, thereby making it difficult to represent a state of marginal instability at Ri ≈ 0.25 (Holmes and Thomas 2015). In contrast, plots of diffusivity versus Ri from observations show a steeper dependence (e.g., Zaron and Moum 2009; Peters et al. 1988). We also find that approximately a third of the parameterized turbulent heat flux in the deep-cycle layer is handled by KPP's surface layer mixing scheme (discussed later in section 4d). Hence deficiencies in KPP's shear mixing scheme may not be the sole reason for the bias in Ri. Here we account for the bias in Ri by treating simulated flows with Ri ≈ 0.4 as being marginally stable.

4. Dynamics of off-equatorial deep-cycle turbulence

A deep cycle of turbulence can only exist in equilibrium in a stratified fluid given a continuous source of shear that acts to reduce Ri; a diurnal trigger that initiates turbulence daily

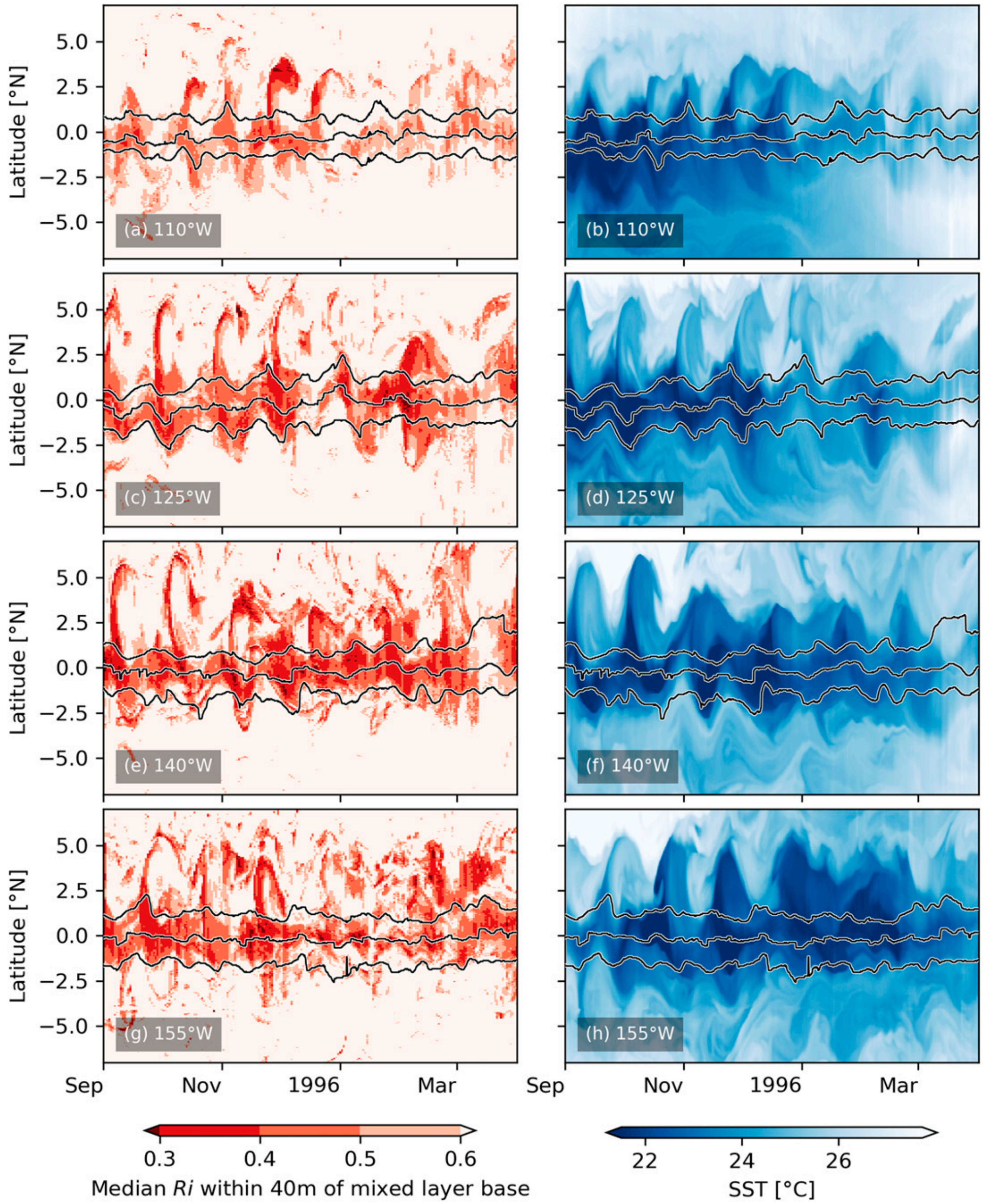

FIG. 3. Low Ri seen in the off-equatorial region at (a) 110°, (c) 125°, (e) 140°, and (g) 155°W between September 1995 and March 1996. (b),(d),(f),(h) Median Ri in the region $z_{\mathrm{MLD}} - 40 \le z \le z_{\mathrm{MLD}}$ daily averaged SST illustrating TIW activity. Black lines on all panels show the EUC maximum and its latitudinal extent defined using the latitudes north and south of the core at which the eastward velocity drops by a factor of 2. The latitudes are determined using u at the depth of maximum eastward velocity.

which may then increase Ri (Smyth et al. 2019); and a process that maintains stratification within the deep-cycle layer. Together these act to maintain the stratified deep-cycle layer in a state of marginal stability. At 0°, 140°W equatorial winds maintain intense zonal shear u_z between the SEC and the EUC and the diurnal trigger may be the nighttime instability of the surface-trapped diurnal warm-layer jet (Pham et al. 2017) or the breaking of downward propagating internal waves triggered by nighttime convection (Wijesekera and Dillon 1991). In contrast, we will see that the simulated marginally stable flow and deep-cycle turbulence at 3.5°N, 110°W is forced by TIW meridional shear v_z (sections 4a, 4b) and the diurnal trigger is the daily descent of the surface mixing layer associated with the weakening of the stabilizing surface buoyancy flux in the afternoon (section 4d). We begin

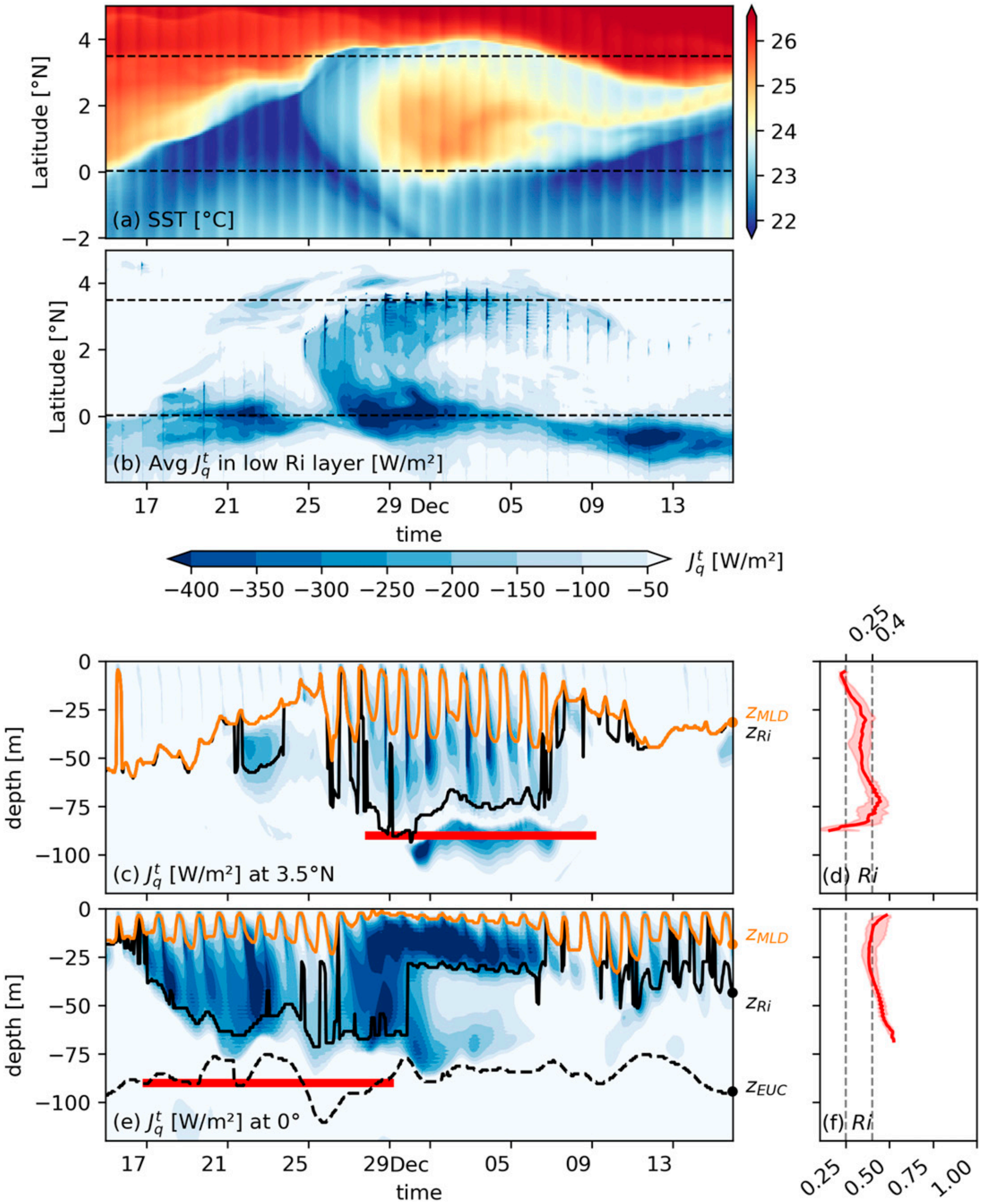

FIG. 4. Deep-cycle turbulence at the equator and 3.5°N. (a),(b) Time–latitude plots of (a) SST and (b) KPP heat flux J_q^t. (c),(e) Time–depth plots of KPP heat flux J_q^t. (d),(f) Median (solid line) and interquartile range (shading) of Ri in the low Ri layer $z_{\mathrm{Ri}} \le z < z_{\mathrm{MLD}}$ for the time period marked by red horizontal lines in (c) and (e), respectively. Dashed vertical lines in (d) and (f) mark Ri = 0.25 and Ri = 0.4. Also shown are the mixed layer depth z_{MLD} (orange line), the depth of the base of the low Ri layer z_{Ri} (solid black line), and the depth of the EUC maximum z_{EUC} (dashed black line).

by describing the shear and stratification structure in the simulated off-equatorial deep-cycle layer (section 4a).

a. *Marginal stability, shear, and stratification in the cold cusp*

The off-equatorial low Ri layer is closely associated with the TIW's cold cusp (Figs. 6a,b, also Figs. 2b,d,e and 3). The contributions of each vector component of the shear as well as the stratification to Ri in the low Ri layer below the cold cusp are decomposed and illustrated by reduced shear $\mathrm{Sh}^2_{\mathrm{red}} = (u_z^2 + v_z^2) - N^2/\mathrm{Ri}_c \gtrsim 0$ (Fig. 6c), where $\mathrm{Ri}_c = 0.4$ instead of the usual 0.25 following the discussion in section 3. The flow in much of the cold cusp is near marginal stability, though the components of $\mathrm{Sh}^2_{\mathrm{red}}$ vary considerably in space and time.

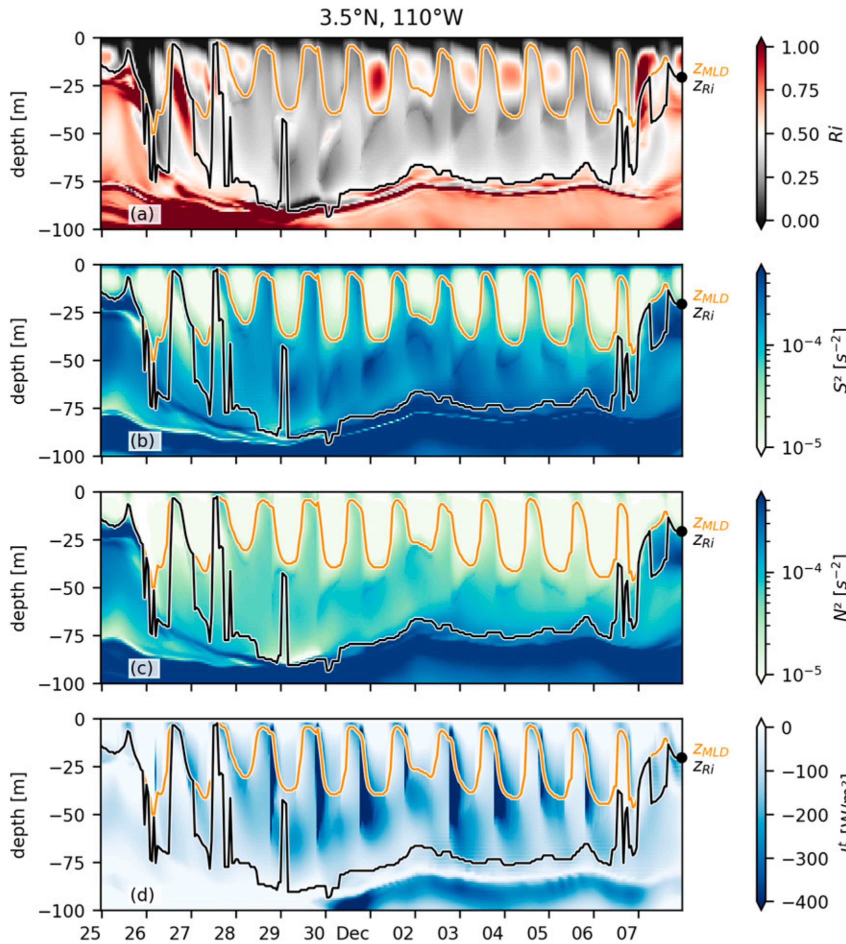

FIG. 5. Daily cycles in (a) Ri, (b) squared shear S^2, (c) buoyancy frequency N^2, and (d) J_q^t at 3.5°N. This time period is a subset of the time period shown in Fig. 4. Also shown are the mixed layer depth z_{MLD} (orange line) and the depth of the base of the low Ri layer z_{Ri} (black line).

Between 1°S and 2°N and behind the cold cusp, the vertical shear of the flow is largely associated with u_z (Fig. 6d). North of 2°N, the shear is largely associated with v_z (Fig. 6e). Combining the shear fields (Figs. 6d,e) with the map of low Ri layer thickness and $\mathrm{Sh}^2_{\mathrm{red}}$ (Figs. 6b,c) suggests that u_z drives the flow toward marginal instability south of 2°N while v_z drives the flow toward marginal instability north of 2°N, in the eastward extension of the cold cusp. Since $\mathrm{Sh}^2_{\mathrm{red}}$ is a linear combination of contributions from N^2, u_z^2 and v_z^2, we split $\mathrm{Sh}^2_{\mathrm{red}}$ into two terms to evaluate whether u_z or v_z is individually large enough to overcome half the stratification necessary to drive the flow toward marginal stability,

$$\mathrm{Sh}^2_{\mathrm{red}} = \left(u_z^2 - \frac{N^2}{2\mathrm{Ri}_c}\right) + \left(v_z^2 - \frac{N^2}{2\mathrm{Ri}_c}\right). \qquad (5)$$

Snapshots of heat flux J_q, reduced shear $u_z^2 + v_z^2 - N^2/\mathrm{Ri}_c$ and the two terms on the RHS of (5) computed using $\mathrm{Ri}_c = 0.4$ are shown in Figs. 7a–l at three different times indicated by vertical dashed lines in Fig. 6. Enhanced turbulence is present in the low Ri layer between z_{MLD} (orange) and z_{Ri} (black). The regions of enhanced turbulence coincide with positive values of reduced shear. Zonal shear u_z is responsible for shear turbulence both at the equator (Figs. 7c,g,k) and in the northward-oriented cold cusp between 0° and 3°N (Figs. 7f,g). The corresponding v_z is weak (Figs. 7h,i). This pattern reverses in the eastward extension of the cold cusp: v_z is strong but u_z is weak between 2° and 4°N (Figs. 7k,l). These three cross sections confirm that u_z acts to force turbulence in the near-equatorial region (1°S–2°N) while v_z forces the off-equatorial deep-cycle turbulence, as inferred from Figs. 6c,d,e.

The stratification N^2 in the low Ri layer below the cold cusp varies by approximately a factor of 2 between the equator and the eastward extension of the cold cusp (Figs. 6f and 10a). This variation is a result of intense mixing seen in the cold cusp as we show later. Next we examine the dynamics underlying the shear field.

b. *Shear forcing of off-equatorial deep-cycle turbulence*

The enhanced off-equatorial v_z is a consequence of the rotation of the horizontal vorticity vector by the TIW's

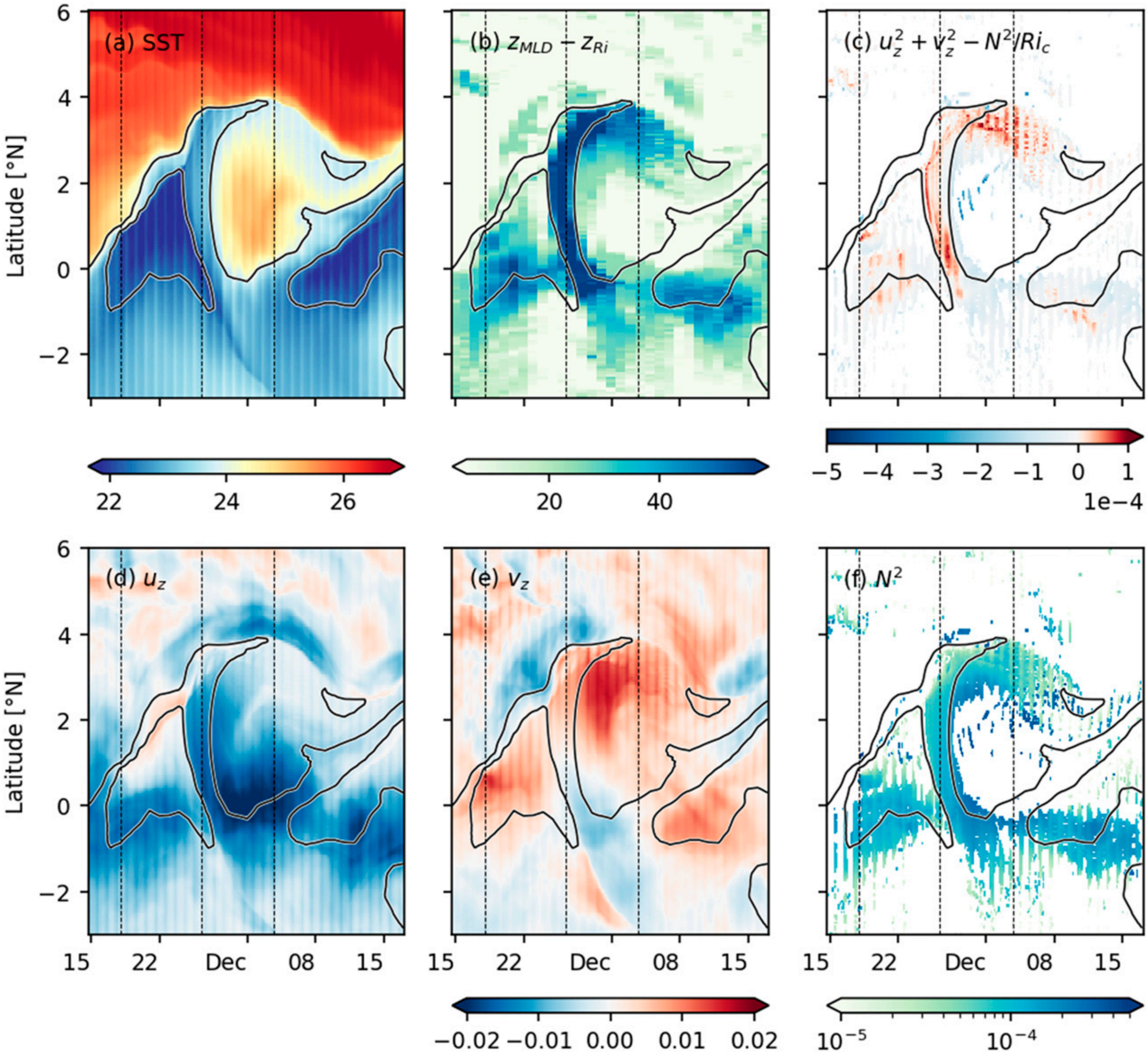

FIG. 6. Time–latitude plots of (a) SST, (b) low Rilow Ri layer thickness, (c) median $\mathrm{Sh}^2_{\mathrm{red}}$ within the low Ri layer (same color bar as in Fig. 7), (d) mean u_z in the top 60 m, (e) mean v_z in the top 60 m, and (f) mean N^2 within the low Ri layer for one TIW. Vertical lines mark time instants presented in Fig. 7. The black contours mark SSTs of 22.4° and 23.5°C.

off-equatorial flow (Fig. 8). Although the flow is unsteady, water parcels follow a vortex-like circular path between 1° and 4°N in the cold cusp (Dutrieux et al. 2008; Holmes et al. 2014), illustrated here by streamlines (green) calculated using velocities relative to an approximate TIW westward translation speed of 0.5 m s^{-1}. The translation speed was determined from Hovmöller plots of SST and 0–60m depth-averaged v at latitudes between 0° and 4°N. The circular path is visible in both latitude–time plane at 110°W and in latitude–longitude plane at 1 December 1995 (Figs. 8a,b). Near-equatorial disturbances propagate faster than off-equatorial disturbances (Kennan and Flament 2000) so the streamlines may be a poor representation of pathlines there. Streamlines pass through the near-equatorial region of high zonal shear, then move northward and eastward approximately parallel to the SST front (black contour; 23.8°C). During this transit the horizontal vorticity vector $\omega^x\hat{\mathbf{i}} + \omega^y\hat{\mathbf{j}} = (w_y - v_z)\hat{\mathbf{i}} + (u_z - w_x)\hat{\mathbf{j}} \approx -v_z\hat{\mathbf{i}} + u_z\hat{\mathbf{j}}$ (black) rotates from pointing southward to pointing westward. This rotation suggests that horizontal vortex tilting transforms ω^y to ω^x during the parcel's transit, i.e., negative u_z in the near-equatorial region is rotated to become positive v_z off the equator.

The dynamics of this transformation can be quantified using the evolution equation for the two shear components.

$$D_t u_z = \underbrace{+u_z v_y}_{\text{STRETCH}} + \underbrace{\zeta v_z}_{\text{TILT1}} \underbrace{- v_x v_z}_{\text{TILT2}} - \underbrace{b_x}_{\text{BUOY}} + \underbrace{F_z^x}_{\text{FRIC}}, \quad (6)$$

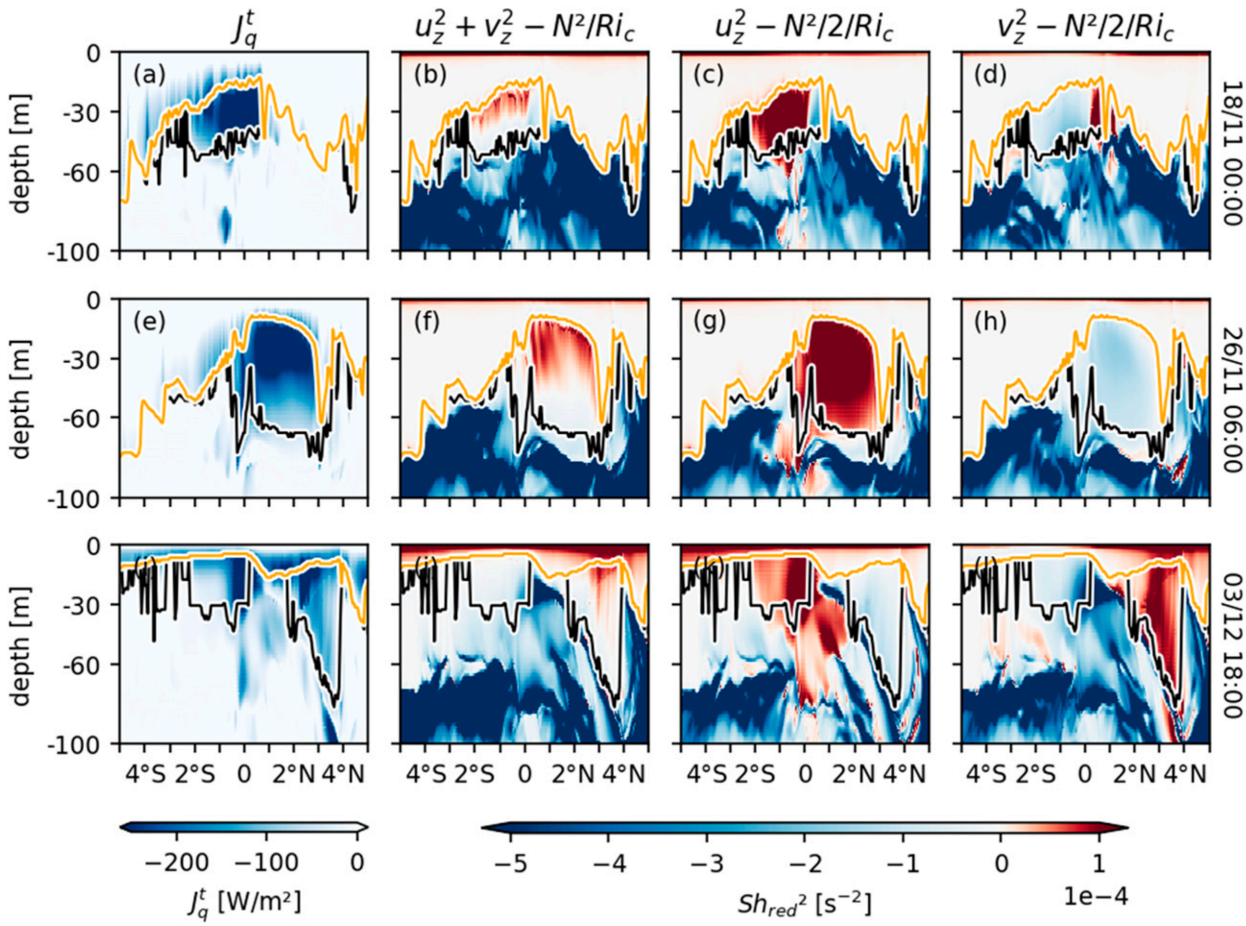

FIG. 7. Zonal shear drives enhanced equatorial turbulence while meridional shear drives enhanced off-equatorial turbulence. In both cases, the turbulence is in the low Ri layer. (a),(e),(i) Turbulent heat flux J_q^t; (b),(f),(j) reduced shear $\mathrm{Sh}_{\mathrm{red}}^2$; (c),(g),(k) zonal shear contribution to $\mathrm{Sh}_{\mathrm{red}}^2$; and (d),(h),(l) meridional shear contribution to $\mathrm{Sh}_{\mathrm{red}}^2$ [see Eq. (5)]. All terms are plotted as a function of depth and latitude at three different time instants: (top) prior to the arrival of the cold cusp, (middle) when the cold cusp is oriented northward, and (bottom) when the cold cusp extends eastward. The time instants are labeled on the right of each row here and are marked by vertical lines in Fig. 6; z_{MLD} and z_{Ri} are marked by orange and black lines, respectively.

$$D_t v_z = +v_z u_x \quad -\zeta u_z \quad -u_y u_z \quad -b_y + F_z^y. \tag{7}$$

Here $\zeta = (f + v_x - u_y)$ is the absolute vertical vorticity, b_x, b_y are baroclinic torque terms, F_z^x, F_z^y are the frictional terms, and $D_t = \partial_t + \partial_x + \partial_y + \partial_z$ is the material derivative. We identify u_z, v_y and v_z, u_x as vortex stretching terms (STRETCH) since a component of horizontal flow divergence v_y (or u_x) acts to stretch or squash a component of horizontal vorticity u_z (or v_z), analogous to vertical divergence w_z stretching or squashing vertical vorticity $v_x - u_y$. We identify $(\zeta - v_x)v_z$ and $(\zeta + u_y)u_z$ as tilting terms since they rotate one component of horizontal vorticity v_z or u_z to modify the other component Du_z/Dt or Dv_z/Dt. The tilting terms are decomposed into two (TILT1, TILT2). TILT1 ≈ 0 because absolute vorticity $\zeta \approx 0$ in the cold cusp (Holmes et al. 2014). The TILT2 terms in Eqs. (6) and (7) do not simply rotate preexisting shear but also act to change the shear magnitude squared S^2 (horizontal enstrophy), which evolves according to

$$\frac{1}{2} D_t S^2 = \underbrace{u_z^2 v_y + v_z^2 u_x}_{\text{STRETCH}} - \underbrace{(u_y + v_x) u_z v_z}_{\text{TILT2}} \\ \underbrace{- u_z b_x - v_z b_y}_{\text{BUOY}} + \underbrace{u_z F_z^x + v_z F_z^y}_{\text{FRIC}}. \tag{8}$$

Note that TILT1 is absent in (8) even if absolute vorticity $\zeta \neq 0$. Taken together, the stretching and TILT2 terms in (8) act to increase S^2 throughout the deep cycle layer (not shown). Here the TILT2 terms appear as flow deformation in the x–y plane $-(u_x + v_y)$ acting to stretch horizontal vortex lines in that plane (u_z, v_z), thereby changing the squared magnitude of horizontal vorticity and vertical shear S^2.

We present both components of vertical shear as well as the evolution terms in the RHS of Eqs. (6) and (7), averaged over the top 60 m, in Fig. 9 along with a contour marking a low Ri layer thickness of 30 m for reference. We focus on the magnitudes of the evolution terms within this 30-m low Ri layer

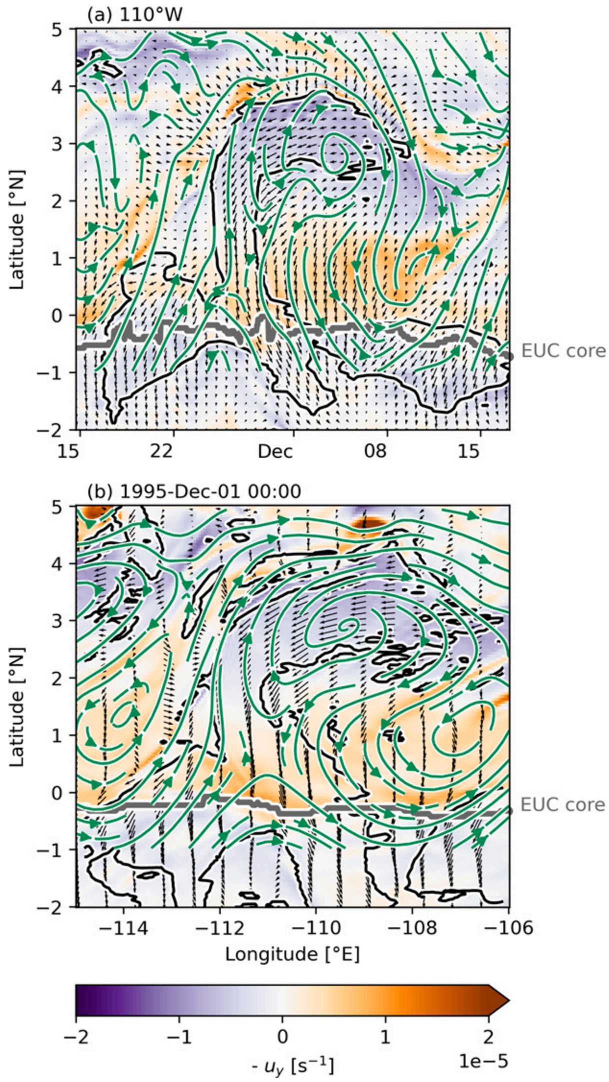

FIG. 8. Depth-averaged horizontal vorticity vectors $\omega^x\hat{\mathbf{i}} + \omega^y\hat{\mathbf{j}} = (w_y - v_z)\hat{\mathbf{i}} + (u_z - w_x)\hat{\mathbf{j}}$ (black vectors) over depth-averaged $-u_y$ (color). Streamlines, in green, are calculated using depth-averaged horizontal velocities with a TIW westward translation speed of $0.5\,\mathrm{m\,s^{-1}}$ removed. All quantities are depth averaged to 60 m. Black contour indicates where the low Ri layer is 30 m thick. The latitude of the EUC core (defined as maximum u averaged between 30 and 120 m) is marked in gray. The horizontal vorticity vector rotates as parcels travel northward from the equator and then eastward. These quantities are presented in (a) time–latitude space at 110°W, time in local time; (b) longitude–latitude space at 0000 UTC 1 Dec 1995.

thickness contour. In the northward-oriented cold cusp between 0° and 3°N, TIW meridional diffluence (positive v_y) stretches the horizontal vorticity through the stretching term, u_z, v_y (Fig. 9c), intensifying u_z and forcing turbulence (Figs. 7e–h) as described by Holmes and Thomas (2015). North of approximately 2°N, the zonal shear weakens and meridional shear intensifies as the horizontal vorticity vector rotates from pointing southward to pointing westward. That is, negative u_z is converted to positive v_z in the northwest corner of the TIW (Fig. 8) through the horizontal vortex tilting terms for both u_z and v_z (TILT2, Figs. 9g,h). The sign of the TILT2 tilting terms within the 30 m contour is such that u_z is increased from a negative value to 0 (its magnitude is decreased) while v_z is increased from 0 to a positive value (Figs. 9a,b). Both tilting by absolute vertical vorticity (TILT1, Figs. 9e,f) and the baroclinic torque (BUOY, Figs. 9i,j) are relatively weak within the 30-m low Ri layer thickness contour. Enhanced turbulence within the 30-m low Ri layer thickness contour acts to decrease S^2 (Figs. 9k,l).

The intensification of u_z in a near-equatorial region by horizontal vortex stretching (Holmes and Thomas 2015), the subsequent rotation of u_z to v_z by the anticyclonic TIW flow u_y (Figs. 9g,h), and the intensification of shear through flow deformation is the continuous shear forcing that forces deep-cycle turbulence in the cold cusp.

c. Stratification in the cold cusp

Stratification N^2 in the low Ri layer decreases as water parcels flow northward and then eastward along the cold cusp (Figs. 6f and 10a). Consider the evolution equation for N^2, ignoring lateral mixing,

$$D_t N^2 = D_t b_z = \underbrace{-u_z b_x - v_z b_y}_{\text{TILT}} - \underbrace{w_z b_z}_{\text{STRETCH}} + \underbrace{\partial_{zz} K_T b_z}_{\text{MIX}}. \quad (9)$$

Integrated over the low Ri layer, the stretching and tilting terms act to increase stratification (STRETCH + TILT, Fig. 10c) while the mixing acts to decrease stratification (MIX, Fig. 10d). In total, these terms act to decrease stratification within most of the low Ri layer (Fig. 10b). Consequently, a relatively weaker shear field can force turbulence in the cold cusp off the equator than on the equator, where stratification is stronger.

d. Simulated trigger of deep-cycle turbulence

As at the equator, turbulence in the low Ri layer must be triggered daily for a diurnal cycle to exist (Fig. 5). How does the KPP scheme model that daily trigger off the equator?

During times of TIW influence, our simulations show some diurnal variation in $H_{0.3}$, the shallowest depth at which $\mathrm{Ri}_b = 0.3$ (section 2a), in the TIW cold cusp off the equator (Fig. 11). However, the base of the KPP boundary layer H_{KPP} is significantly shallower than $H_{0.3}$ during daytime (cf. black and thick red lines in Fig. 11). During daytime, the surface buoyancy forcing is stabilizing and values of H_{KPP} are limited to the Monin–Obukhov scale L_{MO} (section 2a), which is approximately 2.5–5 m (1–2 grid cells deep). After peak sun in the afternoon, L_{MO} deepens to approximately 50–60 m and so does H_{KPP} (Figs. 11b–e). After 1900 local time, the surface heat flux turns destabilizing, so L_{MO} becomes negative, the limiter is removed and H_{KPP} matches $H_{0.3}$ during the night. In this way, the descent of the daytime shear layer in the late afternoon (Smyth et al. 2013) is entirely modeled by the change in surface fluxes (as captured by L_{MO}) rather than a dynamical instability resulting from increased interior shear relative to the stratification (as captured by $H_{0.3}$).

Note that $H_{\mathrm{KPP}} = L_{\mathrm{MO}} > z_{\mathrm{MLD}}$ for approximately an hour (1800–1900 local time) before the onset of convection (vertical white dashed lines). Diffusivities are enhanced within the

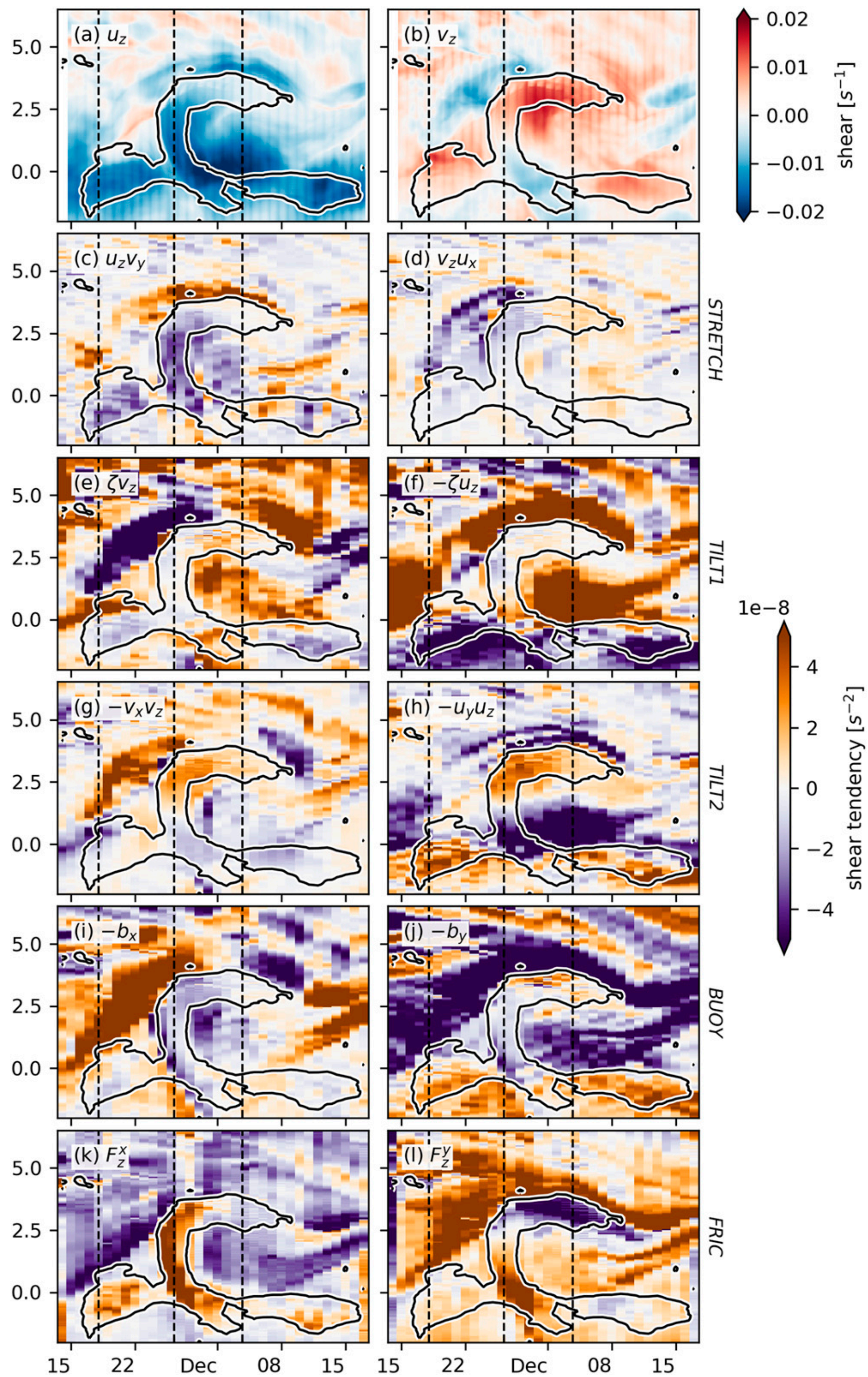

FIG. 9. Terms controlling the evolution of (left) u_z [Eq. (6)] and (right) v_z [Eq. (7)]. All quantities are depth-averaged in the top 60 m. Black contours mark low Ri layer thickness of 30 m for reference. Vertical lines mark the same time stamps as those in Fig. 7.

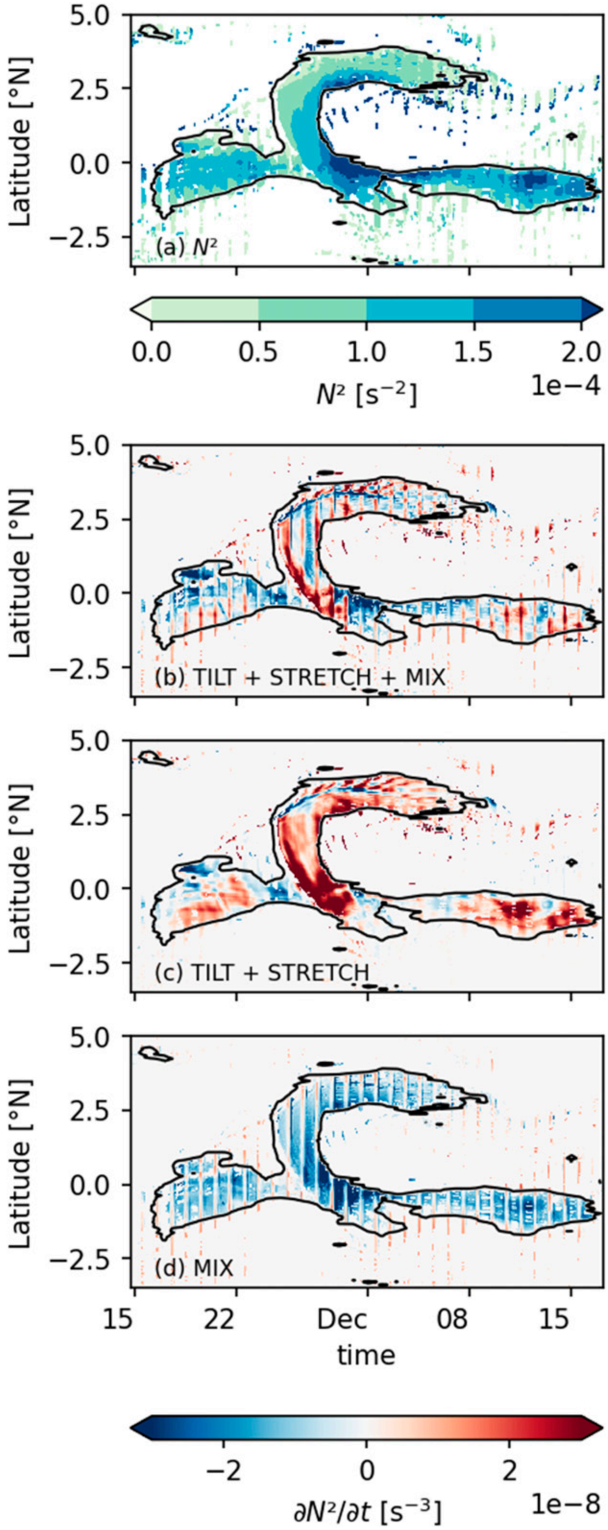

FIG. 10. Time–latitude plots of (a) N^2, and (b)–(d) the stretching, tilting, and mixing terms that contribute to DN^2/Dt [from Eq. (9)] within the low Ri layer. The low Ri layer thickness is larger than 30 m within the black contour.

boundary layer, which includes the stratified water beneath the mixed layer, resulting in large heat fluxes just prior to the onset of nighttime convection. The descent of the boundary layer results in strong parameterized turbulence heat fluxes below the mixed layer where the strong vertical stratification combines with high boundary layer diffusivities (Fig. 11e). Parameterized mixing is also excited in the low Ri layer below H_{KPP}. During the night, Ri increases which in turn reduces J_q^t (Figs. 11b,e). Meanwhile H_{KPP} shoals and approaches z_{MLD} as it descends. When the sun rises, the L_{MO} limiter is activated and the boundary layer shoals to its daytime value of approximately 5 m. Since $L_{MO} < H_{0.3}$, H_{KPP} is set to L_{MO} during the day. Daytime Ri values in the low Ri layer are in the 0.4–0.5 range, so the parameterized shear turbulence is never completely extinguished (KPP enhances diffusivities for Ri < 0.7). The daily cycle then repeats (Fig. 5).

There are two peaks in the parameterized turbulent heat flux J_q^t averaged over the passage of the entire TIW associated with deep-cycle layers at the equator and in the cold cusp (Fig. 12a) Roughly one-third of the total off-equatorial parameterized heat flux in the low Ri layer between 3° and 5°N occurs within the KPP surface boundary layer (Fig. 12a). In contrast, this fraction is negligible near the equator. Equatorial deep-cycle turbulence is almost completely modeled by KPP's interior shear mixing scheme. The difference between the modeled equatorial and off-equatorial deep-cycle turbulence is likely due to the difference in mean N^2, S^2 (Fig. 12b). Off the equator, N^2 is smaller than at the equator by approximately 70%, S^2 is smaller by approximately 40%, and $H_{0.3}$ penetrates deeper below the mixed layer compared to at the equator (Fig. 12c). So a larger fraction of the low Ri layer off the equator is handled by the surface boundary layer scheme. This difference in equatorial and off-equatorial N^2, S^2, $H_{0.3}$ also means that the L_{MO} limiter is more consequential off the equator than at the equator, and may explain why Large and Gent (1999) did not see any sensitivity to the L_{MO} limiter in their equatorial study (note that their calculations did not represent the influence of TIWs; their section 3d). Though the difference between H_{KPP} and z_{MLD} off the equator is small on average (cf. orange and black lines in Fig. 12c), the large diffusivities of the surface boundary layer scheme combine with small but nonzero stratification to yield large heat fluxes off of the equator (e.g., Fig. 11e).

Despite the bias in mean Ri (≈ 0.4 versus the observed 0.25), the average J_q^t at the equator (100–125 W m^{-2}, Fig. 12a) is within a factor of 2 of Warner and Moum's (2019) observational estimate of average $J_q^t \approx 70$–100 W m^{-2} right on the equator during La Niña conditions (when TIWs are active). It is possible that KPP is producing the right turbulent flux but for a flow with Ri ≈ 0.4 instead of Ri ≈ 0.25 by adjusting the diffusivity appropriately. Testing this idea would require a thorough comparison of a simulation covering multiple TIWs with the long-term microstructure observations presented in Warner and Moum (2019).

5. Indirect observational evidence

To our knowledge there is no reported observational evidence for an off-equatorial deep cycle of turbulence associated

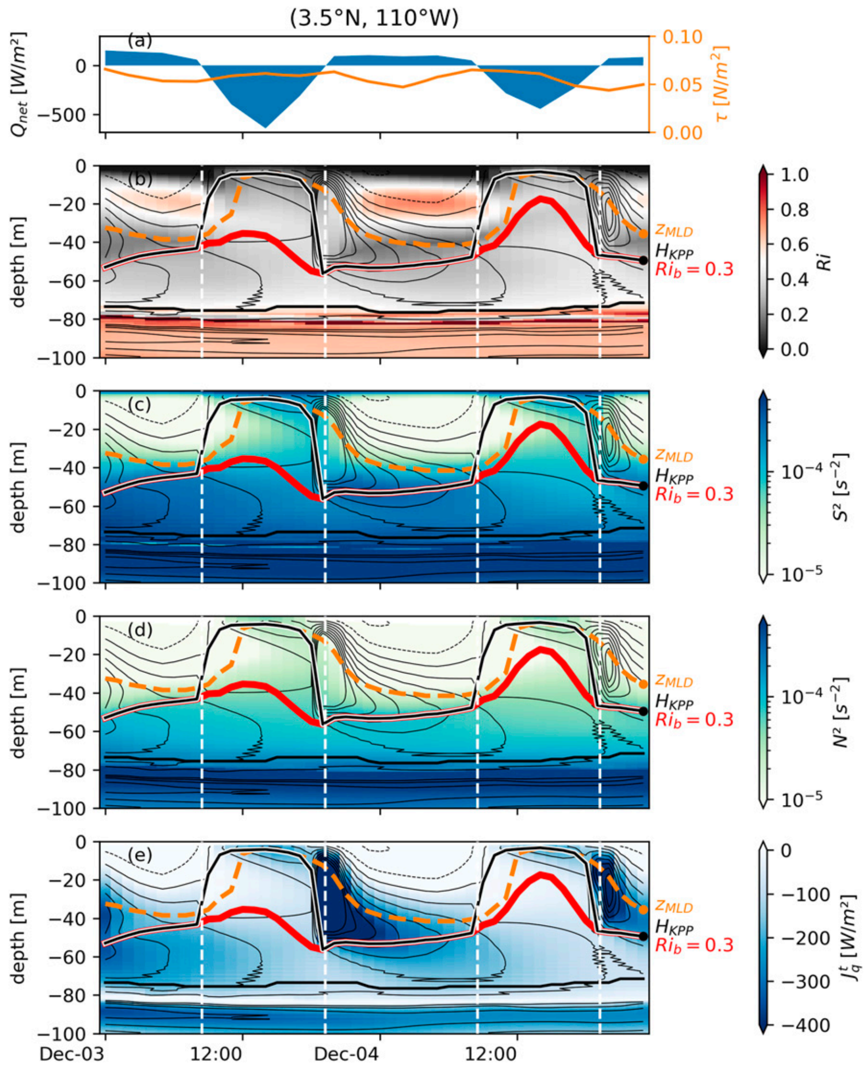

FIG. 11. Turbulence at 3.5°N, 110°W triggered by deepening of the boundary layer in the afternoon. (a) Surface forcing with net surface heat flux in blue and wind stress in orange. (b) Gradient Ri, (c) S^2, (d) N^2, and (e) turbulent heat flux J_q^t. Panels (b)–(e) also show the turbulent heat flux J_q^t (black contours; solid lines are negative, dashed are positive), the mixed layer depth (z_{MLD}, orange dashed line), the KPP boundary layer depth (black line), and the depth at which the bulk Ri_b reaches 0.3 ($H_{0.3}$, red line). Vertical white dashed lines mark time at which net surface heat flux changes sign.

with TIWs. In the absence of direct microstructure measurements, one might look at in situ Ri estimates since marginal stability is detectable using coarse measurements of shear and stratification at least at the equator (Smyth and Moum 2013; Pham et al. 2017). The absence of ADCPs on the off-equatorial TAO moorings prevents replicating the analysis of Smyth and Moum (2013) or Pham et al. (2017). Instead we will use coincident measurements of velocity from shipboard ADCPs and density from CTD casts obtained during cruises that sampled a TIW cold cusp by chance. Cruise CTD and ADCP data were obtained from the CLIVAR and Carbon Hydrographic Data Office (CCHDO) and the Joint Archive for Shipboard ADCP (JASADCP), respectively.

Ri estimated using high-resolution velocity and stratification measurements indicate that deep-cycle turbulence is associated with a Ri distribution with statistical mode 0.25 (2-m velocity bins; Smyth and Moum 2013). The mode remains at 0.25 even when the velocity measurements are significantly degraded to 16-m bins. The Smyth and Moum (2013) observations are limited in that they were taken at a single location (0°, 140°W) for a short period of time (2 weeks) during a period of strong TIW forcing. Guided by their observations, we assume that deep-cycle turbulence everywhere is characterized by a Ri distribution with statistical mode 0.25, and that Ri in the deep-cycle layer can be estimated from relatively coarse observations. Since the

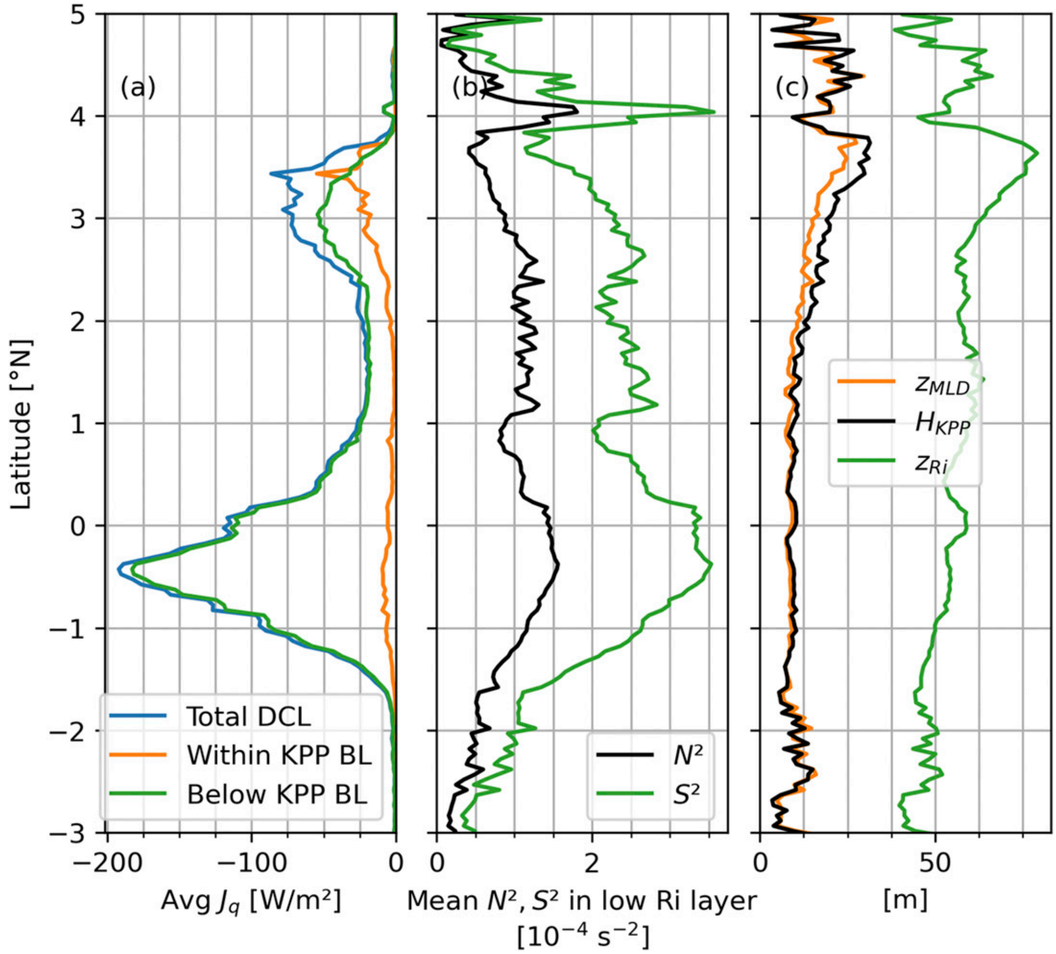

FIG. 12. Meridional profiles of quantities averaged within the low Ri layer at 110°W during the duration of the TIW. (a) J_q^t averaged over time and depth. (b) Mean N^2, S^2 within the low Ri layer. The mean is taken over time and depth axes. (c) Time-mean z_{MLD}, H_{KPP}, and z_{Ri} over the period when the deep cycle is active.

mode is 0.25, we expect the most likely observed Ri value to be 0.25 in a deep-cycle layer.

We infer low values of Ri, less than 1, below the mixed layer both at the equator (as expected) as well as off the equator at 4° and 5°N in profiles from three cruise transects at 110°W through TIWs (Table 1; Fig. 13). We estimate Ri by first averaging the 1-m binned CTD data in the bins used for the ADCP data (either 8- or 10-m bins), and then estimating N^2 and S^2 using centered differences so the gradients are calculated over 16–20 m. Bins where $N^2 < 10^{-6}\,\mathrm{s}^{-2}$ and $S^2 < 10^{-6}\,\mathrm{s}^{-2}$ are excluded. These Ri profiles are presented in Figs. 13b,c,e,f,h,i along with a higher-resolution N^2 profile estimated using 3 m averaged CTD profiles. In general, Ri < 1 off the equator with values close to 0.25 in 3–5 successive bins below the mixed layer (where $N^2 \approx 10^{-5} - 10^{-4}\,\mathrm{s}^{-2}$, Figs. 13c,f,i). As in the model, υ_z is the dominant shear term (not shown). The data in Fig. 13 are noisy but suggest that further examination of such sections might be useful given the lack of moored ADCPs and microstructure data. A more thorough analysis would use all sections at 110°, 125°, and 140°W to estimate a median Ri profile through the TIW cold cusp. This work is ongoing.

6. Summary

We have presented evidence from a high-resolution numerical simulation that TIWs force deep-cycle turbulence off

TABLE 1. Cruise sections at 110°W used for analysis in section 5.

Cruise	Vessel	Dates	Sampling line	ADCP bin size
EP692	R/V *Discoverer*	15 Oct 1992–19 Nov 1992	WOCE PR16	10 m
EP393	R/V *Discoverer*	24 Aug 1993–18 Sep 1993	WOCE PR16	8 m
RB0711	R/V *Ron Brown*	15 Dec 2007–18 Jan 2008	CLIVAR P18N	8 m

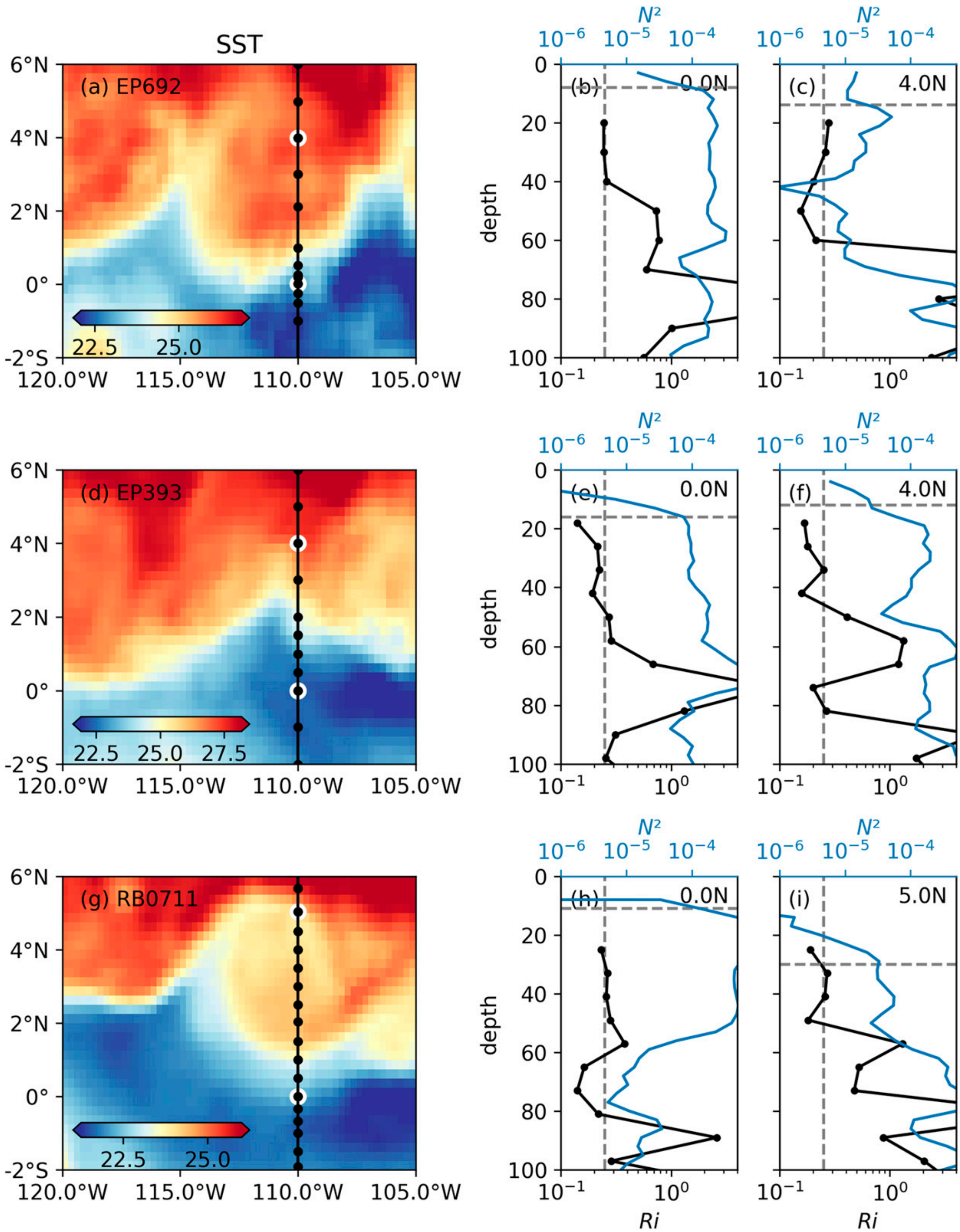

FIG. 13. Indirect evidence for an off-equatorial deep cycle from three cruise transects (Table 1). (a),(d),(g) SST from the daily 0.25° OISST product (Reynolds et al. 2007) with CTD stations marked (note changing color scale). (b),(c),(e),(f),(h),(i) Profiles of Ri (black) and N^2 (blue) at stations marked with white circles in (a), (d), and (g). The vertical line is Ri = 0.25, and the horizontal line is mixed layer depth estimated as the shallowest depth at which the potential density exceeds the shallowest recorded density value by 0.015 kg m^{-3}.

the equator throughout the cold tongue (Figs. 2–5, 11). Horizontal vortex stretching by meridional diffluence v_y of the TIW's flow intensifies preexisting u_z within approximately 2° of the equator (Fig. 9c; Holmes and Thomas 2015). The TIW's anticyclonic flow then rotates the horizontal vorticity anticyclonically while moving fluid away from the equator, converting u_z to v_z in the eastward extension of the cold cusp (Figs. 8 and 9g,h). Flow deformation in the x–y plane also acts to modify the horizontal vorticity in the cold cusp. This continuous stretching and tilting of horizontal vorticity acts to create a region of intense shear and low Ri below the mixed layer in the TIW cold cusp (Fig. 6). The flow regime in the TIW cold cusp is similar to the equatorial flow regime where intense shear (u_z) between the SEC and EUC exists below the mixed layer, except that the shear is now associated with meridional flow (v_z, Fig. 7). There is a daily cycle of turbulence in the off-equatorial low Ri layer that is associated with a downward descending shear layer in the afternoon (Fig. 5).

Although the simulated off-equatorial deep cycle has many qualitative similarities to the equatorial deep cycle, some details differ. Notably the descending surface boundary layer, which triggers deep-cycle turbulence, frequently descends with the Monin–Obukhov (MO) depth L_{MO} as the stabilizing surface buoyancy flux weakens in the afternoon off of the equator. At the equator, in contrast, the descent of the stable surface boundary layer during the afternoon is usually (approximately two-thirds of the time) controlled by the bulk Richardson number, which is increasing momentum in the near-surface layer, or occurs with the onset of convection in the evening (as in Large and Gent 1999; Pham et al. 2017). Preliminary experiments without the L_{MO} limiter indicate that the limiter can significantly influence the diurnal cycle of vertical mixing, consistent with the results of this paper (cf. L_{MO} and $H_{0.3}$ in Fig. 11e). However, future work is required to clarify whether these differences persist once feedbacks develop, and how the L_{MO} limiter impacts the model solution mean state, and the daily cycle of turbulence. In any case, the deepening boundary layer results in mixing in the low Ri layer beneath the MLD leading to daily cycles of parameterized turbulence, Ri, S^2 and N^2 in the low Ri layer in the cold cusp off the equator (Figs. 5 and 11; section 4d). Approximately one-third of the simulated off-equatorial turbulent heat flux is within the surface boundary layer, in contrast to the equatorial deep-cycle where the boundary layer accounts for a very small fraction of turbulent heat flux (Fig. 12a).

The accuracy of KPP's simulation of these details of the off-equatorial deep cycle needs to be evaluated with LES simulations that account for the large-scale lateral TIW shear forcing. Most published LES simulations of deep-cycle turbulence do not account for lateral momentum and buoyancy flux forcing terms, and none that we know of account for TIW forcing explicitly. Observational evidence for an off-equatorial deep cycle is restricted to a small number of Ri profiles from opportunistic cruise transect data within a TIW cold cusp (Fig. 13). Similarly the horizontal vortex stretching and tilting dynamics described here and in Holmes and Thomas (2015) also need to observationally verified. Hence, there is a need for high-resolution microstructure observations to validate the current MITgcm and future LES simulations.

Deep-cycle turbulence transports heat absorbed by the near-surface ocean during daytime to depths deeper than the base of the convective mixed layer, keeping it away from reabsorption by the atmosphere during convection the following night. In doing so, deep-cycle turbulence helps keep the sea surface cool, enabling significant heat uptake by the eastern equatorial Pacific cold tongue while it remains in approximate thermal equilibrium. Our simulations indicate that this effective subduction of heat is taking place over an area larger than what might be expected from shear turbulence associated with SEC–EUC shear, i.e., poleward of the 3°S–3°N region (Figs. 2 and 3). Yet direct microstructure measurements have mostly been made at the equator. Our results, and the associated uncertainties, emphasize the need to constrain the magnitude, the dynamics, and the long term impact of off-equatorial turbulence in the eastern Pacific cold tongue.

Acknowledgments. This work was funded by National Oceanic and Atmospheric Administration Contract NA18OAR4310408 from the Climate Program Office. The MITgcm simulation output used for this paper is available on NCAR's Digital Asset Services Hub (DASH) repository (https://dashrepo.ucar.edu/). We have provided daily averages for much of the domain (doi:10.5065/6qa0-v481); 4-hourly output along latitudinal sections at longitudes 110°, 125°, 140°, and 155°W (doi:10.5065/6qa0-v481); and hourly fields for the TIW that is the focus of this paper (doi:10.5065/3kb5-g350). We acknowledge many fruitful discussions with Dr. Frank Bryan and Dr. Anna-Lena Deppenmeier. The authors thank W. Smyth and an anonymous reviewer for their kind comments and valuable suggestions. We would like to acknowledge high-performance computing support from Cheyenne (doi:10.5065/D6RX99HX) provided by NCAR's Computational and Information Systems Laboratory, sponsored by the National Science Foundation. This material is based upon work supported by the National Center for Atmospheric Research, which is a major facility sponsored by the National Science Foundation under Cooperative Agreement No. 1852977. Analysis was greatly helped by the use of the xarray Python package (Hoyer and Hamman 2017). Code to reproduce Figs. 2–12 is available at doi:10.5281/zenodo.4535984.

REFERENCES

Adcroft, A., C. N. Hill, J.-M. Campin, J. Marshall, and P. Heimbach, 2004: Overview of the formulation and numerics of the MIT GCM. *Seminar on Recent Developments in Numerical Methods for Atmospheric and Ocean Modelling*, Reading, United Kingdom, ECMWF, 11 pp., https://www.ecmwf.int/node/7642.

Chelton, D. B., F. J. Wentz, C. L. Gentemann, R. A. de Szoeke, and M. G. Schlax, 2000: Satellite microwave SST observations of transequatorial tropical instability waves. *Geophys. Res. Lett.*, **27**, 1239–1242, https://doi.org/10.1029/1999GL011047.

Computational And Information Systems Laboratory, 2019: Cheyenne: SGI ICE XA Cluster (Climate Simulation Laboratory). National Center for Atmospheric Research, https://doi.org/10.5065/D6RX99HX.

Dutrieux, P., C. E. Menkes, J. Vialard, P. Flament, and B. Blanke, 2008: Lagrangian study of tropical instability vortices in the Atlantic. *J. Phys. Oceanogr.*, **38**, 400–417, https://doi.org/10.1175/2007JPO3763.1.

Gregg, M. C., H. Peters, J. C. Wesson, N. S. Oakey, and T. J. Shay, 1985: Intensive measurements of turbulence and shear in the equatorial undercurrent. *Nature*, **318**, 140–144, https://doi.org/10.1038/318140a0.

Holmes, R. M., and L. N. Thomas, 2015: The modulation of equatorial turbulence by tropical instability waves in a regional ocean model. *J. Phys. Oceanogr.*, **45**, 1155–1173, https://doi.org/10.1175/JPO-D-14-0209.1.

——, and ——, 2016: Modulation of tropical instability wave intensity by equatorial Kelvin waves. *J. Phys. Oceanogr.*, **46**, 2623–2643, https://doi.org/10.1175/JPO-D-16-0064.1.

——, ——, L. Thompson, and D. Darr, 2014: Potential vorticity dynamics of tropical instability vortices. *J. Phys. Oceanogr.*, **44**, 995–1011, https://doi.org/10.1175/JPO-D-13-0157.1.

——, J. D. Zika, and M. H. England, 2019: Diathermal heat transport in a global ocean model. *J. Phys. Oceanogr.*, **49**, 141–161, https://doi.org/10.1175/JPO-D-18-0098.1.

Hoyer, S., and J. J. Hamman, 2017: Xarray: N-D labeled arrays and datasets in Python. *J. Open Res. Software*, **5**, 10, https://doi.org/10.5334/jors.148.

Inoue, R., R.-C. Lien, and J. N. Moum, 2012: Modulation of equatorial turbulence by a tropical instability wave. *J. Geophys. Res.*, **117**, C10009, https://doi.org/10.1029/2011JC007767.

——, R. Lien, J. N. Moum, R. C. Perez, and M. C. Gregg, 2019: Variations of equatorial shear, stratification, and turbulence within a tropical instability wave cycle. *J. Geophys. Res. Oceans*, **124**, 1858–1875, https://doi.org/10.1029/2018JC014480.

Johnson, G. C., B. M. Sloyan, W. S. Kessler, and K. E. McTaggart, 2002: Direct measurements of upper ocean currents and water properties across the tropical Pacific during the 1990s. *Prog. Oceanogr.*, **52**, 31–61, https://doi.org/10.1016/S0079-6611(02)00021-6.

Kennan, S. C., and P. J. Flament, 2000: Observations of a tropical instability vortex. *J. Phys. Oceanogr.*, **30**, 2277–2301, https://doi.org/10.1175/1520-0485(2000)030<2277:OOATIV>2.0.CO;2.

Large, W. G., and P. R. Gent, 1999: Validation of vertical mixing in an equatorial ocean model using large eddy simulations and observations. *J. Phys. Oceanogr.*, **29**, 449–464, https://doi.org/10.1175/1520-0485(1999)029<0449:VOVMIA>2.0.CO;2.

——, and S. G. Yeager, 2009: The global climatology of an interannually varying air–sea flux data set. *Climate Dyn.*, **33**, 341–364, https://doi.org/10.1007/s00382-008-0441-3.

——, J. C. McWilliams, and S. C. Doney, 1994: Oceanic vertical mixing: A review and a model with a nonlocal boundary layer parameterization. *Rev. Geophys.*, **32**, 363, https://doi.org/10.1029/94RG01872.

Legeckis, R., 1977: Long waves in the eastern equatorial Pacific Ocean: A view from a geostationary satellite. *Science*, **197**, 1179–1181, https://doi.org/10.1126/science.197.4309.1179.

Lien, R.-C., D. R. Caldwell, M. C. Gregg, and J. N. Moum, 1995: Turbulence variability at the equator in the central Pacific at the beginning of the 19911993 El Niño. *J. Geophys. Res.*, **100**, 6881, https://doi.org/10.1029/94JC03312.

——, E. A. D'Asaro, and C. E. Menkes, 2008: Modulation of equatorial turbulence by tropical instability waves. *Geophys. Res. Lett.*, **35**, L24607, https://doi.org/10.1029/2008GL035860.

Liu, C., L. Fang, A. Köhl, Z. Liu, W. D. Smyth, and F. Wang, 2019: The subsurface mode tropical instability waves in the equatorial Pacific Ocean and their impacts on shear and mixing. *Geophys. Res. Lett.*, **46**, 12 270–12 278, https://doi.org/10.1029/2019GL085123.

—— X. Wang, Z. Liu, A. Köhl, W. D. Smyth, and F. Wang, 2020: On the formation of a subsurface weakly sheared laminar layer and an upper thermocline strongly sheared turbulent layer in the eastern equatorial Pacific: Interplays of multiple time scale equatorial waves. *J. Phys. Oceanogr.*, **50**, 2907–2930, https://doi.org/10.1175/JPO-D-19-0245.1.

Lyman, J. M., D. B. Chelton, R. A. deSzoeke, and R. M. Samelson, 2005: Tropical instability waves as a resonance between equatorial Rossby waves. *J. Phys. Oceanogr.*, **35**, 232–254, https://doi.org/10.1175/JPO-2668.1.

Marshall, J., A. Adcroft, C. Hill, L. Perelman, and C. Heisey, 1997: A finite-volume, incompressible Navier stokes model for studies of the ocean on parallel computers. *J. Geophys. Res.*, **102**, 5753–5766, https://doi.org/10.1029/96JC02775.

Menkes, C. E. R., J. G. Vialard, S. C. Kennan, J.-P. Boulanger, and G. V. Madec, 2006: A modeling study of the impact of tropical instability waves on the heat budget of the eastern equatorial Pacific. *J. Phys. Oceanogr.*, **36**, 847–865, https://doi.org/10.1175/JPO2904.1.

Moum, J. N., and D. R. Caldwell, 1985: Local influences on shear-flow turbulence in the equatorial ocean. *Science*, **230**, 315–316, https://doi.org/10.1126/science.230.4723.315.

——, R.-C. Lien, A. Perlin, J. D. Nash, M. C. Gregg, and P. J. Wiles, 2009: Sea surface cooling at the equator by subsurface mixing in tropical instability waves. *Nat. Geosci.*, **2**, 761–765, https://doi.org/10.1038/ngeo657.

——, A. Perlin, J. D. Nash, and M. J. McPhaden, 2013: Seasonal sea surface cooling in the equatorial Pacific cold tongue controlled by ocean mixing. *Nature*, **500**, 64–67, https://doi.org/10.1038/nature12363.

Pei, S., T. Shinoda, W. Wang, and R. Lien, 2020: Simulation of deep cycle turbulence by a global ocean general circulation model. *Geophys. Res. Lett.*, **47**, e2020GL088384, https://doi.org/10.1029/2020GL088384.

Peters, H., M. C. Gregg, and J. M. Toole, 1988: On the parameterization of equatorial turbulence. *J. Geophys. Res.*, **93**, 1199, https://doi.org/10.1029/JC093iC02p01199.

——, ——, and T. B. Sanford, 1994: The diurnal cycle of the upper equatorial ocean: Turbulence, fine-scale shear, and mean shear. *J. Geophys. Res.*, **99**, 7707, https://doi.org/10.1029/93JC03506.

Pham, H. T., W. D. Smyth, S. Sarkar, and J. N. Moum, 2017: Seasonality of deep cycle turbulence in the eastern equatorial Pacific. *J. Phys. Oceanogr.*, **47**, 2189–2209, https://doi.org/10.1175/JPO-D-17-0008.1.

Philander, S. G. H., 1976: Instabilities of zonal equatorial currents. *J. Geophys. Res.*, **81**, 3725–3735, https://doi.org/10.1029/JC081i021p03725.

Pujiana, K., J. N. Moum, and W. D. Smyth, 2018: The role of turbulence in redistributing upper-ocean heat, freshwater, and momentum in response to the MJO in the equatorial Indian Ocean. *J. Phys. Oceanogr.*, **48**, 197–220, https://doi.org/10.1175/JPO-D-17-0146.1.

Qiao, L., and R. H. Weisberg, 1995: Tropical instability wave kinematics: Observations from the tropical instability wave experiment. *J. Geophys. Res.*, **100**, 8677, https://doi.org/10.1029/95JC00305.

Ray, S., A. T. Wittenberg, S. M. Griffies, and F. Zeng, 2018: Understanding the equatorial Pacific cold tongue time-mean heat budget. Part I: Diagnostic framework. *J. Climate*, **31**, 9965–9985, https://doi.org/10.1175/JCLI-D-18-0152.1.

Reynolds, R. W., T. M. Smith, C. Liu, D. B. Chelton, K. S. Casey, and M. G. Schlax, 2007: Daily high-resolution-blended analyses for sea surface temperature. *J. Climate*, **20**, 5473–5496, https://doi.org/10.1175/2007JCLI1824.1.

Schudlich, R. R., and J. F. Price, 1992: Diurnal cycles of current, temperature, and turbulent dissipation in a model of the equatorial upper ocean. *J. Geophys. Res.*, **97**, 5409–5422, https://doi.org/10.1029/91JC01918.

Smyth, W. D., and J. N. Moum, 2013: Marginal instability and deep cycle turbulence in the eastern equatorial Pacific Ocean. *Geophys. Res. Lett.*, **40**, 6181–6185, https://doi.org/10.1002/2013GL058403.

——, ——, L. Li, and S. A. Thorpe, 2013: Diurnal shear instability, the descent of the surface shear layer, and the deep cycle of equatorial turbulence. *J. Phys. Oceanogr.*, **43**, 2432–2455, https://doi.org/10.1175/JPO-D-13-089.1.

——, J. D. Nash, and J. N. Moum, 2019: Self-organized criticality in geophysical turbulence. *Sci. Rep.*, **9**, 3747, https://doi.org/10.1038/s41598-019-39869-w.

Strutton, P. G., J. P. Ryan, and F. P. Chavez, 2001: Enhanced chlorophyll associated with tropical instability waves in the equatorial Pacific. *Geophys. Res. Lett.*, **28**, 2005–2008, https://doi.org/10.1029/2000GL012166.

Thorpe, S. A., and Z. Liu, 2009: Marginal instability? *J. Phys. Oceanogr.*, **39**, 2373–2381, https://doi.org/10.1175/2009JPO4153.1.

Tsujino, H., and Coauthors, 2018: JRA-55 based surface dataset for driving ocean–sea-ice models (JRA55-do). *Ocean Modell.*, **130**, 79–139, https://doi.org/10.1016/j.ocemod.2018.07.002.

Wang, W., and M. J. McPhaden, 1999: The surface-layer heat balance in the equatorial Pacific Ocean. Part I: Mean seasonal cycle. *J. Phys. Oceanogr.*, **29**, 1812–1831, https://doi.org/10.1175/1520-0485(1999)029<1812:TSLHBI>2.0.CO;2.

——, and ——, 2000: The surface-layer heat balance in the equatorial Pacific Ocean. Part II: Interannual variability. *J. Phys. Oceanogr.*, **30**, 2989–3008, https://doi.org/10.1175/1520-0485(2001)031<2989:TSLHBI>2.0.CO;2.

Warner, S. J., and J. N. Moum, 2019: Feedback of mixing to ENSO phase change. *Geophys. Res. Lett.*, **46**, 13 920–13 927, https://doi.org/10.1029/2019GL085415.

——, R. M. Holmes, E. H. M. Hawkins, M. S. Hoecker-Martínez, A. C. Savage, and J. N. Moum, 2018: Buoyant gravity currents released from tropical instability waves. *J. Phys. Oceanogr.*, **48**, 361–382, https://doi.org/10.1175/JPO-D-17-0144.1.

Wenegrat, J. O., and M. J. McPhaden, 2015: Dynamics of the surface layer diurnal cycle in the equatorial Atlantic Ocean (0°, 23°W). *J. Geophys. Res. Oceans*, **120**, 563–581, https://doi.org/10.1002/2014JC010504.

Wijesekera, H. W., and T. M. Dillon, 1991: Internal waves and mixing in the upper equatorial Pacific Ocean. *J. Geophys. Res.*, **96**, 7115, https://doi.org/10.1029/90JC02727.

Yoder, J. A., S. G. Ackleson, R. T. Barber, P. Flament, and W. M. Balch, 1994: A line in the sea. *Nature*, **371**, 689–692, https://doi.org/10.1038/371689a0.

Zaron, E. D., and J. N. Moum, 2009: A new look at Richardson number mixing schemes for equatorial ocean modeling. *J. Phys. Oceanogr.*, **39**, 2652–2664, https://doi.org/10.1175/2009JPO4133.1.